# ~~Modelling sun-induced~~ Using different radiative transfer schemes for solar-induced chlorophyll fluorescence (SIF) in evergreen ~~conifer~~ coniferous forests~~with a terrestrial biosphere model~~

Tea Thum[1], Javier Pacheco-Labrador[2], Mika Aurela[1], Alan Barr[3], Marika Honkanen[1], Bruce Johnson[3], Hannakaisa Lindqvist[1], Troy Magney[4], Mirco Migliavacca[5], Zoe Amie Pierrat[6, 7], Tristan Quaife[8], Jochen Stutz[9], and Sönke Zaehle[10]

[1]Finnish Meteorological Institute, Helsinki, Finland
[2]Environmental Remote Sensing and Spectroscopy Laboratory (SpecLab), Spanish National Research Council (CSIC), Madrid, Spain
[3]University of Saskatchewan, Canada
[4]Department of Forest Management, University of Montana, Missoula, MT, USA
[5]European Commission, Joint Research Centre, Ispra (VA), Italy
[6]Jet Propulsion Laboratory, Pasadena, California, USA
[7]Department of Geography, University of Santa Barbara, California, USA
[8]National Centre for Earth Observation, University of Reading, Reading, The United Kingdom
[9]University of California Los Angeles, California, USA
[10]Max Planck Institute for Biogeochemistry, Jena, Germany

**Correspondence:** Tea Thum (tea.thum@fmi.fi)

**Abstract.** Solar-induced chlorophyll fluorescence (SIF) is a small light signal emitted during the initial steps of photosynthesis and can be observed across scales (from photosystem level to ~~satellites~~satellite observation footprints). To be able to model SIF, we need to understand the mechanistic processes (including both physical and biological) leading to the observed SIF signal. In this ~~work~~study, we implemented a representation of SIF emission and transmission processes into the terrestrial biosphere model QUINCY ('QUantifying Interactions between terrestrial Nutrient CYcles and the climate system'). We tested the model across three different boreal coniferous forests located in North America and Europe that have eddy covariance derived $CO_2$ fluxes and tower-based SIF observations. We ~~find that alternative~~ found that different SIF radiative transfer approaches (one based on mSCOPE, one on two-stream radiative transfer model L2SM, and one empirically based) ~~overestimate~~ overestimated the SIF signal, but ~~show~~ showed no large differences in the timing of their seasonal and diurnal predictions. The two-stream radiative transfer model approach, L2SM, provided stable performance while being comparatively computationally efficient. ~~We find that our~~ Our parameterization for sustained non-photochemical quenching ~~is~~ was important for successfully simulating the timing of the SIF seasonal cycle. However, our parameterization did not ~~work equally well across~~ perform equally well at all three sites, likely because of different temperature regimes at ~~the~~ each sites. We further evaluated the potential of remote sensing -based SIF from TROPOMI (the TROPOspheric Monitoring Instrument) to provide accurate information on SIF and found that it ~~can~~ could potentially be used in model development. This study ~~illustrates~~ demonstrated the usefulness of observations at ~~different~~ various spatial scales and the linkages between SIF and GPP and their seasonal development at three different evergreen forest sites.

*Copyright statement.* TEXT

## 1 Introduction

The northern latitudes are experiencing stronger climatic change than the rest of the globe (Rantanen et al., 2022). Boreal forests located in these regions are an important part of the global carbon cycle and the biomass located in boreal forests is estimated to be 264.9 ± 10.5 (Pan et al., 2024). Boreal forests are characterized by strong seasonality in environmental conditions, with harsh winter conditions and shoulder seasons when air and soil temperature and light availability drive the spring recovery and autumn drawdown of vegetation (Tanja et al., 2003; Thum et al., 2009; Vesala et al., 2010). The photosynthetic activity of evergreen forests in these ecosystems cannot be easily tracked by reflectance-based remote sensing alone, as the greenness is partially decoupled from the rate of photosynthesis (Walther et al., 2016). Solar-induced chlorophyll fluorescence (SIF) observations have proven to be more reliable proxies for tracking photosynthesis in these ecosystems (Pierrat et al., 2024) . Challenging conditions have led evergreen trees to develop different coping mechanisms. Sustained non-photochemical quenching (NPQ) is one of them and it increases in winter, at the same time as the capacity of photosystem II decreases (Adams et al., 2014). NPQ is a pH-independent mechanism associated with the retention of the xanthophyll cycle pigments zeaxanthin and antheraxanthin and allows the needles to dissipate the incoming radiation as heat (Demmig-Adams et al., 2014) .

Sustained NPQ can only be estimated from the active chlorophyll fluorescence (ChlF) observations, i.e. when a set of saturating light pulses are delivered to a leaf under dark- and light-adapted conditions. Therefore, it cannot be directly obtained from passive SIF observations that take place under natural illumination conditions, although progress is being made towards optical sensing of NPQ (Van Wittenberghe et al., 2024). Including description of sustained NPQ in large scale terrestrial biosphere models (TBMs) was started by Raczka et al. (2019), who used the state of acclimation, represented by a delayed temperature sum developed by Mäkelä et al. (2004) in the parameterization. Climate-induced changes will alter the seasonal cycle of vegetation, and the ability to have optical data to track photosynthetic activity is very helpful in understanding the changes in the carbon cycle. Another feature of boreal forests is that they contain a lot of their carbon belowground (Bradshaw and Warkentin, 2015). The use of terrestrial biosphere models (TBMs) makes it possible to study the entire carbon balance and is therefore an important tool for studies at high latitudes.

Space-based observations have the ability to can monitor the entire Earth's surface, and advances in remote sensing methods and satellite technology are providing provide more data streams that can be used in for carbon cycle studies (Schimel et al., 2019). The ability to observe SIF sun-induced chlorophyll fluorescence (SIF) from space has led to numerous applications (Mohammed et al., 2019). SIF is linked to the light reactions of photosynthesis and can therefore provide information on terrestrial $CO_2$ uptake (Porcar-Castell et al., 2021). Early research on SIF showed that the relationship between SIF and photosynthesis (gross primary productivity, GPP) is linear when measured from space (Frankenberg et al., 2011; Sun et al., 2017) (Frankenberg et al., 2011; Guanter et al., 2012; Joiner et al., 2011, 2013; Sun et al., 2017). Subsequent work has challenged this assumption, showing that the relationship between SIF and GPP is more complex (Damm et al., 2015; Magney et al., 2020;

Martini et al., 2022; Sun et al., 2023b) even when using space-based observations (Balde et al., 2023). Therefore, process-based approaches are useful for understanding the mechanistic drivers of the SIF-GPP relationship.

Observations of leaf-level chlorophyll fluorescence (ChlF) have been widely used in plant physiological research for decades. Consequently, there is a thorough understanding of the mechanisms governing leaf-level ~~fluorescence~~ ChlF (Baker, 2008; Maxwell and Johnson, 2000). When photons are absorbed by plant leaves, they have three main non-damage pathways: they can be used for photochemistry, emitted as ChlF, or dissipated as heat. Since these three pathways coexist, the amount of NPQ affects the relationship between ChlF and photochemistry. In ChlF, a small fraction of photons are re-emitted after giving up some of their energy at higher wavelengths (SIF spectrum is between 650 and 840 nm, as in Fig. 1) (Porcar-Castell et al., 2021). SIF is ChlF that takes place under natural illumination conditions, and measuring it is referred to as a passive measurement of ChlF.

When moving from the leaf level to the canopy level, the interpretation of the measured signal becomes more challenging. Scattering and re-absorption of ChlF take place within the canopy (Van Der Tol et al., 2019). These processes influence how much of the SIF signal located in the red part of the spectrum is absorbed compared to the near-infrared (NIR) (also called "far-red") region. The structural effects of the canopy play an important role in the transmission of the emitted SIF signal within the canopy (Paul-Limoges et al., 2018) and explain the anisotropy of the observed SIF at the top of the canopy (Joiner et al., 2020; Malenovský et al., 2021). The soil ~~will also contribute~~ also contributes to the SIF signal observed at the top of the canopy, as observed signals include contributions from both vegetation and soil components (Yang et al., 2025b). The variability in radiative transfer through the canopy creates challenges for interpreting the measured SIF signal. By using radiative transfer and biological modelling, mechanistic drivers of the SIF signal can be disentangled, improving our interpretation of SIF (Damm et al., 2015).

The use of SIF in ~~carbon cycle~~ vegetation modeling has become widespread. The first leaf-level description for ChlF was in ~~FluorMod~~ FluorModLeaf (Miller et al., 2005). A wide-spread leaf level model that was further developed from ~~FluorMod~~ FluorModLeaf was within the Soil Canopy Observation of Photosynthesis and Energy fluxes (SCOPE) model (van der Tol et al., 2009). SCOPE is a site level model which combines the Farquhar photosynthesis model with a detailed radiative transfer scheme based on SAIL ~~(van der Tol et al., 2009)~~(van der Tol et al., 2009; Verhoef, 1984). A newer leaf level model, that was also implemented in SCOPE, was published a few years later (van der Tol et al., 2014) and further developments have also been made (Vilfan et al., 2016, 2018). The SCOPE model has been widely used in many applications, e.g. studying relationship of GPP and SIF in different ecosystems and under different fertilization treatments as well as water stress effects (e.g., Damm et al., 2015; Martini et al., 2019; Wang et al., 2023; Zhang et al., 2018). Recent model developments also allow the use of SIF to estimate GPP (Gu et al., 2019). These methods utilize the link between measured SIF and light reactions of photosynthesis and how these observations provide a link for actual electron transport from photosystem II to photosystem I. The model by Johnson and Berry (2021) has a tight coupling between photosynthesis and ChlF and allows for ~~bi-directional~~ two-directional modelling, estimating SIF from GPP and vice versa.

~~TBMs~~ Terrestrial biosphere models (TBMs) are large-scale models used to study the biogeochemical cycles and land–atmosphere interactions. They can be run at a large scale (regional and global), but site-scale simulations are still possible. The

modelling community has implemented SIF models in TBMs with varying degrees of complexity. For example, Koffi et al. (2015) augmented the Biosphere Energy Transfer Hydrology (BETHY) model with the full SCOPE model. Lee et al. (2015) used a simple scheme to account for radiative transfer in the CLM implementation. Bacour et al. (2019) built a SCOPE emulator for an implementation in the ORCHIDEE model. Qiu et al. (2019) implemented SIF to the BEPS model and emphasized the importance of accounting for scattering in the modelling, and also data assimilation studies have been done with the BEPS model (Wang et al., 2021).

These different approaches balance simplifying the complex physical phenomenon of radiative transfer in plant canopies against the length of the simulation time. However, full 1D radiative transfer based on the SCOPE model is too computationally demanding for many large scale applications (Sun et al., 2023a) and some modelling teams have needed to use parameterizations instead of the full model (Miyauchi et al., 2025). The computational burden becomes even more relevant in different data assimilation approaches ~~(Norton et al., 2019; MacBean et al., 2018)~~(Norton et al., 2019). An empirical approach used in some studies would be worth investigating (Liu et al., 2020; Zeng et al., 2019). ~~A two-stream radiative transfer~~ One way to simplify the calculation of SIF signal~~has been considered to be computationally tangible (Sun et al., 2023a) and a recent model (Quaife, 2025) enables calculation of SIF, since it~~ 's radiative transfer would be to use a two-stream radiative transfer model (Sun et al., 2023a). A recent two-stream radiative transfer model (Quaife, 2025) describes radiative transfer of emission originating from the canopy ~~.~~ and therefore enables calculation of SIF signal's radiative transfer. The TBM studies mentioned used spaceborne data from Greenhouse gases Observing SATellite (GOSAT) (Kuze et al., 2009) and Orbiting Carbon Observatory (OCO)-2 (Frankenberg et al., 2014).

~~This work aims~~ The northern latitudes are experiencing stronger climatic change than the rest of the globe (Rantanen et al., 2022) . Boreal forests located in these regions are an important part of the global carbon cycle (Pan et al., 2024). Boreal forests are characterized by strong seasonality in environmental conditions, with harsh winter conditions and shoulder seasons when air and soil temperature and light availability drive the spring recovery and autumn drawdown of vegetation (Tanja et al., 2003; Thum et al., 200 . The photosynthetic activity of evergreen forests in these ecosystems cannot be easily tracked by reflectance-based remote sensing alone, as the greenness is partially decoupled from the rate of photosynthesis (Walther et al., 2016). SIF observations have proven to be more reliable proxies for tracking photosynthesis in these ecosystems (Pierrat et al., 2024). Challenging conditions have led evergreen trees to develop different coping mechanisms. Sustained non-photochemical quenching (NPQ) is one of them and it increases in winter, at the same time as the capacity of photosystem II decreases (Porcar-Castell et al., 2008; Porcar-Caste . NPQ is a pH-independent mechanism associated with the retention of the xanthophyll cycle pigments zeaxanthin and antheraxanthin and allows the needles to dissipate the incoming radiation as heat (Demmig-Adams et al., 2014).

Sustained NPQ can only be estimated from the active ChlF observations, i.e. when a set of saturating light pulses are delivered to a leaf under dark- and light-adapted conditions. Therefore, it cannot be directly obtained from passive SIF observations, although progress is being made towards optical sensing of NPQ (Van Wittenberghe et al., 2024). Including description of sustained NPQ in large scale TBMs was started by Raczka et al. (2019), who used the state of acclimation, represented by a delayed temperature sum developed by Mäkelä et al. (2004) in the parameterization. Climate-induced changes

will alter the seasonal cycle of vegetation, and the ability to have optical data to track photosynthetic activity is very helpful in understanding the changes in the carbon cycle.

The goal of this work was to improve the ~~modelling of ChlF~~ ChlF modelling so that a TBM can fully exploit the ~~potential of the different data streams associated with SIF and pave the way for data assimilation approaches~~information provided by the ChlF related observations at different scales to improve our understanding of ecosystem processes related to biogeochemical cycles. Our objectives were 1) to test different radiative transfer approaches for SIF and 2) to assess the role of sustained NPQ in modelling. The research questions of our study are therefore:

- Which radiative transfer model calculation methods were sufficiently robust for reliable SIF model predictions?
- How could we account for the influence of sustained non-photochemical quenching in the modeled SIF signal?
- What was the benefit of in-situ observations versus satellite observations of SIF in model development?

To answer these questions, we run simulations of TBM QUINCY ('QUantifying Interactions between terrestrial Nutrient CYcles and the climate system') and compared them with tower observations of SIF at three coniferous evergreen sites that experience a strong seasonal cycle with harsh winters. In addition, we tested how ~~TROPOMI satellite~~ spaceborn TROPOspheric Monitoring Instrument (TROPOMI) instrument (on board the Sentinel-5 Precursor (S5P) satellite) (Guanter et al., 2021) data capture the seasonal cycle at ~~one~~ two of these sites and how its magnitude differs from the ~~site-level observations .~~ simulation results. The novel aspects of this study include using different radiative transfer schemes with one model, analyzing both red and far-red region observations from the tower observations of SIF, having sites in two different continents and having approaches that either include the SIF signal attenuation inside the leaf or not. Including both red and far-red regions in the analysis will help to evaluate potential challenges that the simulations will have in the red region, a fact that will become more relevant with new satellite missions covering whole SIF spectrum.

## 2 Materials and methods

### 2.1 Site descriptions and observations

The three study sites were Niwot Ridge (US-NR1) ~~(Bowling et al., 2018; Burns et al., 2015; ?)~~(Bowling et al., 2018; Burns et al., 2015; Ma , USA, Saskatchewan (CA-Obs), Canada (Pierrat et al., 2021, 2022a) and Sodankylä (FI-Sod), Finland (Thum et al., 2007; Knorr et al., 2025). All of these sites are evergreen coniferous forests. The Canadian and Finnish sites are in the boreal zone, and Niwot Ridge is a subalpine forest. Further details about the sites are given in Table 1. All sites have eddy covariance flux observations as well as a tower-mounted in-situ SIF instrument. The Sodankylä site is part of the ICOS network (https://www.icos-cp.eu/) and the North American sites are part of AmeriFlux (https://ameriflux.lbl.(gov/).

All of these sites exhibit strong seasonal cycle in vegetation activity, but it differs due to variations in latitude and elevation. The forest in CA-Obs experienced a strong seasonal cycle with low levels of photosynthetic activity between October and March. Although US-NR1 is located at a lower latitude than the other study sites, the high elevation conditions result in

**Table 1.** The site characteristics of the three forests. LAI is one-sided and average value over summertime. Air temperature is annual average.

| Abbreviation | Location (lat, lon) | Species and age (yrs) | Period | LAI ($m^2\ m^{-2}$) | Air temp. (°C) | SIF instrument |
|---|---|---|---|---|---|---|
| CA-Obs | 53.99, -105.12 | Black spruce (>100) | 2019-2020 | 3.8 | 1.3 | PhotoSpec |
| FI-Sod | 67.36°, 26.64° | Scots pine (90) | 2021 | 1.3-1.4 | 0.3 | FloX |
| US-NR1 | 40.03°, -105.55° | Mixed evergreen coniferous (>100) | 2017-2018 | 3.8–4.2 | 2.7 | PhotoSpec |

pronounced seasonal cycle, including below freezing winters. The forest at US-NR1 is photosynthetically active from May to September, with the shoulder season to winter occurring in October and December, and spring recovery occurring in April and May. FI-Sod is located 100 km north of the Arctic Circle. Therefore, the winter radiation drops to zero, and temperatures are low. Spring recovery occurs in April and May. The photosynthetically active period is from June to August and photosynthesis ceases in September and October.

### 2.2 SIF and $CO_2$ flux observations at the sites

At the North American sites, SIF was observed with PhotoSpec (Grossmann et al., 2018) in two different spectral regions. The red region is between 680 and 686 nm, and the far-red region is between 745 and 758 nm. These observations were made with a 2D scanning telescope. The retrieval method is based on the Fraunhofer line method (Grossmann et al., 2018). The field of view (FOV) is 0.7°. At US-NR1 a typical measurement included a scan from nadir to the horizon in 0.7° steps at two different azimuth direction ~~(?)~~(Magney et al., 2019a). At CA-Obs three vertical scans at three different directions (35°W, 0°N, 35°E) were done in sequence (Pierrat et al., 2021). The PhotoSpec retrievals were filtered by having an Normalized Difference Vegetation Index (NDVI) based threshold to ensure that only observations of vegetation were used. In this study we averaged over all the observations. More details of these observations can be found in ~~?~~ Magney et al. (2019a) (US-NR1) and Pierrat et al. (2021) (CA-Obs). At US-NR1, observations were available from June 2017 until June 2018. At CA-Obs we used observations for whole years 2019 and 2020. In spring 2019 the eddy covariance observations were out of commission and until mid-2019 the GPP data was based on gap–filling.

In Sodankylä, the observations were made ~~with a~~ using a a FloX box (JB Hyperspectral Devices, Düsseldorf, Germany) (https://www.jb-hyperspectral.com/products/flox/). ~~The FloX box~~ These observations were used to retrieve the SIF in the $O_2B$ band at 687 nm in the red region and the$O_2A$ band at 760 nm in the far-red region. The retrieval method used to process the data was the improved Fraunhofer line method (Alonso et al., 2008; Cendrero-Mateo et al., 2019). ~~We~~ In our study, we used close to nadir observations from June 2021 until the end of ~~2021 in our study~~the year. The FOV is 25°. The different wavelengths of the retrieved SIF signals by the instruments are shown in Fig. 1, along with the SIF spectrum from observations of Scots pine needles in Hyytiälä, southern Finland ~~(Magney et al., 2019b)~~(Magney and Frankenberg, 2019; Magney et al., 2019b).

~~The~~ Net ecosystem exchange of $CO_2$ ~~fluxes were measured above the canopy. At FI-Sod, measurements were made at 25 m with a Gill HS-50 sonic anemometer (Gill Instruments, Lymington, UK) and a LiCor LI-7200 gas analyzer (LiCor Inc.,~~

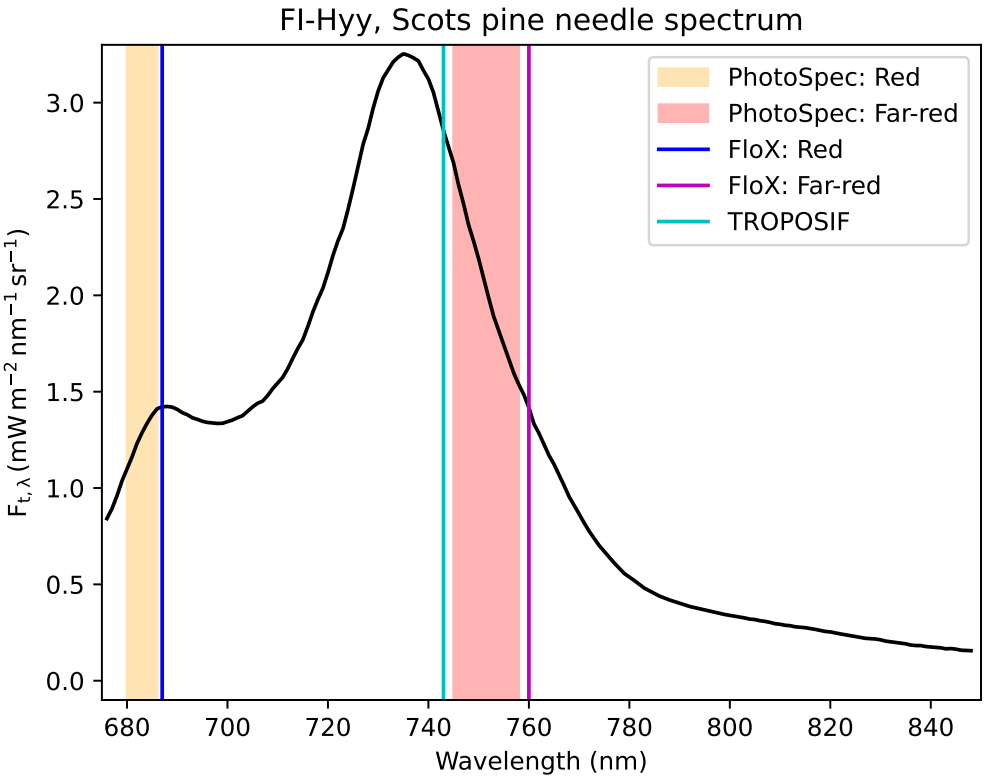


**Figure 1.** SIF emission spectrum for Scots pine located in the southern boreal zone (from ~~Magney et al. (2019b)~~ Magney and Frankenberg (2019)) with wavelength regions of the observations. The lines indicate the bands for which the SIF signal was retrieved for the FloX observations and TROPOMI (TROPOSIF) and the shaded regions indicate the wavelength regions for which the SIF with the PhotoSpec was retrieved.

~~Lincoln, NE, USA) (Knorr et al., 2025). At~~ was measured by the eddy covariance method. At CA-Obs the measurement height was 25 m, and the anemometer was CSAT3 (Campbell Scientific Inc., Logan, UT, USA) and the gas analyzer LI-7200 (Pierrat et al., 2021). At US-NR1 measurements were made at 21.5 m height with the CSAT3 and an LI-6262 gas analyzer ~~(?).~~ (Magney et al., 2019a). At FI-Sod, measurements were made at 25 m with a Gill HS-50 sonic anemometer (Gill Instruments, Lymington, UK) and a LiCor LI-7200 gas analyzer (LiCor Inc., Lincoln, NE, USA) (Knorr et al., 2025). Flux partitioning and gap–filling at CA-Obs was done as described in Barr et al. (2004) and at US-NR1 using the Reichstein et al. (2005) method with the R package REddyProc (Wutzler et al., 2018). Gap–filling and partitioning of the measured net ecosystem exchange flux to gross primary production (GPP) and total ecosystem respiration was done at FI-Sod following Aurela et al. (2015). ~~Flux partitioning and gap–filling at CA-Obs was done as described in Barr et al. (2004) and at US-NR1 using the Reichstein et al. (2005) method with the R package REddyProc (Wutzler et al., 2018)~~In Sodankylä, the fraction of absorbed

photosynthetically active radiation (fAPAR) was measured using PQS1 instruments (Kipp & Zonen; Netherlands) (Knorr et al., 2025) . Four of these sensors were installed below the canopy. These observations, together with aboveground canopy observations, were used to calculate fAPAR.

### 2.3 Remote sensing observations of SIF by TROPOMI

The ~~TROPOspheric Monitoring Instrument (TROPOMI )~~ TROPOMI is aboard the Copernicus Sentinel-5P mission and has been providing data since 2018 ~~(Guanter et al., 2021)~~(Köhler et al., 2018). TROPOMI has global continuous spatial sampling with daily revisit times, because it has a nearly sun-synchronous orbit with a repeat cycle of 16 days and a wide swath of 2600 km (Köhler et al., 2018). The pixel size at nadir was 3.5 x 7.5 $km^2$ at the beginning of the mission and 3.5 x 5.5 $km^2$ after August 2019 (Guanter et al., 2021). ~~The instrument's near infrared band 6 covers the spectral range between 725-775 nm, with a full width at half maximum (FWHM) = 0.38 nm, making it suitable for retrieving far-red SIF (Köhler et al., 2018).~~ We used the TROPOSIF product derived from the 743-758 nm window, at 743 nm (Guanter et al., 2021). The retrieval methodology is based on the Fraunhofer line in-filling principle (Plascyk and Gabriel, 1975) and a data-driven method is used (Guanter et al., 2015).

In this study we used 0.5° x 0.5° sampling area around two study sites, CA-Obs and FI-Sod~~, corresponding to about~~ . This corresponds to an area of approximately 56 km x 33 km at CA-Obs. ~~We~~ According to the MODIS MCD12C1 from 2018 (Friedl and Sulla-Menashe, 2022), the land cover for CA-Obs in this region is 65 % woody savannah and 26 % evergreen needleleaf forest, with minor contributions from mixed forests and croplands. For FI-Sod the land cover was 83 % woody savannah and 17 % savannah. We also tested using a smaller sampling area around the region, extending 0.25° around the site. For this smaller region the land cover around CA-Obs was 45 % evergreen forest and 53 % woody savannah, with small contribution of mixed forests. For the FI-Sod site the smaller region had 92 % woody savannah and 8 % of savannah. We did not use TROPOMI data for US-NR1 because TROPOMI observations only covered part of the in situ observational period. TROPOMI's Level 2 cloud fraction product was applied for a strict cloud filtering, removing all SIF data for which the cloud fraction exceeded 0.2~~.~~ , as recommended by Guanter et al. (2021). In our analysis we used daily averages that we had calculated from instantaneous values.

### 2.4 Model description of QUINCY

The QUantifying Interactions between terrestrial Nutrient CYcles and the climate system (QUINCY) model is a terrestrial biosphere model ~~(TBM)~~ that can be run on a single site or larger, such as regional or global, scales. ~~Here we give a~~ QUINCY uses plant functional types (PFTs) to describe different ecosystems. In site level simulations, each site is described by a single PFT. Canopy can have up to ten layers. A brief description of the model ~~,~~ is provided here; further details can be found in Thum et al. (2019).

The complete version of QUINCY has fully coupled carbon, energy, nitrogen and phosphorus cycles. The model has a modular structure that allows only some parts of the model to be run. We used the canopy module, which calculates fast biophysical processes of the model, including stomatal conductance, photosynthesis and radiative transfer within the canopy.

Influence of soil is considered so that water uptake is constrained by soil moisture given a prescribed, ~~plant functional type~~ PFT -specific root profile. Leaf area index (LAI) and leaf nitrogen content are prescribed with a constant value in the canopy module (otherwise these would be calculated prognostically inside the model). ~~The depth (in terms of LAI) of the canopy layers increases exponentially towards the lower canopy layers, of which there are a maximum of ten layers. The nitrogen gradient decreases with canopy depth according to observations (Niinemets et al., 1998).~~ Leaf stoichiometry, i.e. the nitrogen to carbon ratio, is fixed in the canopy module. The calculation of leaf chlorophyll from the leaf nitrogen is described in Section S1.1.

Photosynthesis is calculated according to Kull and Kruijt (1998). This approach is based on the biochemical model of Farquhar et al. (1980), but instead of the regular implementation of having the minimum of the two branches limiting photosynthesis (light-limited rate of photosynthesis and carboxylation capacity limited rate), the amount of light-saturated region in the leaf is taken into account. In the non-light-saturated part, photosynthesis is calculated using the light-limited rate of photosynthesis based on the maximum electron transport rate parameter $J_{max,25}$ (the parameter has been scaled to 25 °C). For the light-saturated part, photosynthesis is calculated as the minimum of electron transport rate-limited photosynthesis and the carboxylation capacity limited photosynthesis (determined by the maximum carboxylation capacity parameter $V_{c(max),25}$).

Photosynthesis is calculated separately for sunlit and shaded leaves in each canopy layer and coupled to the stomatal conductance (Medlyn et al., 2011), described in Section S1.2. Evergreen trees in cold environments adapt their photosynthesis during the shoulder seasons as described in Section S1.3. ~~The~~

### 2.4.1 Radiative transfer in QUINCY

The depth (in terms of LAI) of the canopy layers increases exponentially towards the lower canopy layers, of which there are a maximum of ten layers. The nitrogen gradient decreases with canopy depth according to observations (Niinemets et al., 1998) , but is not connected to the leaf optical properties in the current model formulation. The fraction of sunlit and shaded leaves are calculated using the radiative transfer scheme based on the two-stream approach of Spitters (1986), and extended to include canopy albedo, clumping and attenuation of the shortwave backscatter from the ground. Radiative transfer is calculated separately for the visible (300-700 nm) and near-infrared (700-3000 nm) bands. Leaf reflectance is calculated based on the PFT-specific single leaf scattering albedo (SSA). Leaf transmissivity is assumed to be equal to reflectivity ~~. Clumping~~and absorptance is one minus SSA. Clumping index ($\Omega$), non-random distribution of leaf elements, is described according to Campbell and Norman (1998).~~

~~The onset of photosynthesis for evergreen coniferous forests is delayed as a function of air temperature in QUINCY (Thum et al., 2019). The use of a constant temperature response for the photosynthesis parameters $J_{max,25}$ and $V_{c(max),25}$ has been shown to predict too early spring recovery in boreal coniferous forests (Thum et al., 2008). Therefore, a more accurate representation of delayed spring onset of these parameters has been adapted from Mäkelä et al. (2019) and parameterized using several sites from the FLUXNET database (NOA, 2007). The formulation for the state of acclimation (SOA) ($S$) is (Mäkelä et al., 2004)~~:

$$\frac{dS}{dt}\Omega = \frac{1}{\tau_{soa}}\Omega_0/(T_{air} - S\Omega_0 + (1-\Omega_0)) \times e^{-k_{csf} \times acos(\gamma^*)^{\phi_{crown}}}, \quad (1)$$

where ~~$\tau_{soa}$ is a time constant (114 ) and $T_{air}$ is the air temperature. Therefore, $S$ is a delayed temperature sum. It is used to calculate a delay factor ($\beta_{soa}$) for photosynthesis (used as a multiplier for the parameters $V_{c(max,25)}$~~ $\Omega_0$ and $\phi_{crown}$ are the PFT-specific clumping factor at nadir (0.5 for conifers) and ~~$J_{max,25}$ as described in Thum et al. (2019)) :~~

~~$$\beta_{soa} = \frac{1}{1 + e^{b(S-T_s)}}$$~~

~~where $b$ (°C$^{-1}$) and $T_s$ (°C)are parameters, set to -0.5 °C$^{-1}$~~ crown shape factor (2.19 for conifers), respectively, and ~~5.0 °C, respectively~~$k_{csf}$ is a correction factor (value 2.2). A seasonal cycle of Ω at FI-Sod site is shown in Fig. S1. Because all equations for leaf reflection and absorption coefficients are only valid for high solar elevation, the true zenith angle ($\gamma$) is constrained to values larger than 10° ($\gamma^*$). Otherwise the leaves are assumed to be distributed hemispherically. The soil albedo is set to a literature value (Bonan, 2008) for the visible and near infrared regions.

### 2.5 ~~Leaf level model of chlorophyll fluorescence~~

### 2.5 Models for the radiative transfer of the SIF signal

~~We applied the widely used leaf level model for steady-state leaf chlorophyll fluorescence developed by van der Tol et al. (2014) . It is part of the Soil Canopy Observation, Photochemistry and Energy fluxes (SCOPE)model (van der Tol et al., 2009) and its derivatives, such as mSCOPE (Yang et al., 2017). Here, we briefly introduce the equations of this leaf model to clarify its implementation in QUINCY. We could not directly follow the implementation in SCOPE, because QUINCY has a different formulation for the photosynthesis model, which is described in section 2.4. For a detailed description of the model, see van der Tol et al. (2014).~~ The leaf chlorophyll fluorescence yield was calculated using the model developed by (van der Tol et al., 2014). Its equations are shown in SI, Section 1.4. We did not change any of this model's default parameter values, and these parameters were kept constant for all the sites. The only change to the standard implementation of the model was caused by the different Farquhar et al. model formulation adapted to QUINCY, but this did not require any additional parameters.

~~The ChlF pathway of using excitations in the leaves will be denoted by $F$, photochemistry by $P$. Heat dissipation is divided into a constitutive thermal dissipation, denoted by $D$, and an energy-dependent heat dissipation, denoted by $N$, and this is NPQ. $D$ is present in dark-adapted plants, while $N$ is more variable and controlled by the electron transport of the photosystems. Below we introduce the reversible NPQ and in the next Section 2.7 also a formulation for the sustained NPQ, which is an additive term to the reversible NPQ.~~

~~The rate coefficients ($K$) express the probability of different rates of excitation and can be used to express the yield:~~

$$\Phi_P = \frac{K_P}{\sum K}$$

$$\Phi_F = \frac{K_F}{\sum K}$$

$$\Phi_D = \frac{K_D}{\sum K}$$

$$\Phi_N = \frac{K_N}{\sum K}$$

$$\sum K = K_P + K_F + K_D + K_N$$

These rates are mutually exclusive, and therefore the yield of all processes is :

$$\Phi_P + \Phi_F + \Phi_D + \Phi_N = 1$$

The rate coefficient $K_F$ is constant and $K_D$ depends on the air temperature ($T_{air}$ in C)as estimated from measurements by (van der Tol et al., 2014):

$$K_D = MAX(0.8738, 0.0301\frac{1}{C^\circ} * T_{air} + 0.0773)$$

while $K_N$ and $K_P$ are influenced by the metabolic state of the leaves .

According to Genty et al. (1989), the $\Phi_P$ at the steady state can be calculated from the ratio of the variable fluorescence ($F'_m - F_t$) to the maximum fluorescence in light ($F'_m$), as

$$\Phi_P = \frac{F'_m - F_t}{F'_m}$$

where $F_t$ is the steady-state fluorescence. Yields can be expected to follow the Genty relationship:

$$\Phi_{F_t} = (1 - \Phi_P)\Phi_{F'_m}$$

where $\Phi_{F_t}$ is the steady-state fluorescence yield and $\Phi_{F'_m}$ is the yield of maximum fluorescence in light, obtained with a saturating pulse in the PAM observations. To evaluate $\Phi_{F'_m}$, we note that the rate coefficient of photosynthesis $K_P$ goes to zero with the saturating light pulse, since then all the open PSII reaction centers are closed by the pulse. Because of this and Eq. (**??**) we get

$$\Phi_{F'_m} = \frac{K_F}{K_F + K_D + K_N}$$

and here only $K_N$ is unknown. van der Tol et al. (2014) developed an experimental relationship to relate $K_N$ to the changes in $\Phi_P$. The $K_N$ that controls $F'_m$ must be related to the relative decrease in the photochemical yield. To achieve this, a factor $x$ is defined which is zero when photochemistry is working at full efficiency and one when photochemistry is completely absent. This is

$$x = 1 - \frac{\Phi_P}{\Phi_P^0}$$

where $\Phi_P^0$ is the maximum photochemical yield which can be observed under dark adapted and low light conditions.

In the original SCOPE formulation , the constraint imposed on $\Phi_P$ is calculated as the fraction of actual electron transport compared to potential electron transport. Since QUINCYhas a different formulation for photosynthesis, we calculated the limitation on $\Phi_P$ as a fraction of actual electron transport compared to the case where the whole leaf would be light limited, i.e. there would be no saturated region at all. In principle, our solution is similar, although the formulation of the photosynthesis model is slightly different.

The escape fraction describes how much of the emitted SIF signal reaches the top of the canopy. The steady-state chlorophyll fluorescence is total canopy SIF can be expressed using the escape fraction $f_{esc}$ as (Sun et al., 2017):

$$\Phi_{F_t} = (1 - \Phi_P^0 + x\Phi_P^0)\Phi_{F'_m}$$

The empirical relationship between $x$ and $K_N$ is (van der Tol et al., 2014)

$$K_N = \frac{(1+\beta)x^\alpha}{\beta + x^\alpha} K_N^0$$

where the parameters are $K_N^0 = 2.48$, $\alpha = 2.83$ and $\beta = 0.114$. These are for the standard conditions, while the van der Tol et al. (2014) also gives parameter values for water-limited conditions. This is the reversible part of the $K_N$, which we will refer to as $K_{N_{rev}}$ in the following section.

The chlorophyll fluorescence yield can be used to calculate the SIF emission per leaf layer $SIF_{cl}$,

$$SIF_{cl} = Sun_{frac} PPFD_{sun} PAR \cdot fAPAR \cdot \Phi_{F_t,sun} + (1 - Sun_{frac}) PPFD_{sha} \Phi_{F_t,sha} F_t \cdot f_{esc} \quad (2)$$

where $PPFD_{sun}$ is the absorbed SIF is the observed SIF, PAR is the photosynthetically active radiation(PAR) for the sunlit leaves, $PPFD_{sha}$ for the shaded leaves and $Sun_{frac}$, fAPAR is the fraction of the sunlit leaves. The $\Phi_{F_t,sun}$ is the fluorescence

yield calculated for the sunlit leaves and $\Phi_{F_{t,sha}}$ for the shaded leaves. Sections 2.5.1-2.5.3 will describe the different ways in which this emission has been scaled up to absorbed PAR and $\Phi_{F_t}$ is the chlorophyll fluorescence yield. This section introduces three different ways to calculate the radiative transfer of SIF in the canopy level.

Variables of leaf level chlorophyll fluorescence model, including values held constant. All of these variables are unitless. Variable name (unit) Symbol Value Rate coefficient for photosynthesis (-) $K_P$ - Rate coefficient for fluorescence (-) $K_F$ 0.05 Rate coefficient for constitutive heat dissipation (-) $K_D$ Eq. (**??**) Rate coefficient for energy-dependent heat dissipation (-) $K_N$ - Yield for photosynthesis (-) $\Phi_P$ - Yield for fluorescence (-) $\Phi_F$ - Yield for constitutive heat dissipation (-) $\Phi_D$ - Yield for energy-dependent heat dissipation (-) $\Phi_N$ - Maximum fluorescence in light (-) $F'_m$ - Steady-state fluorescence (-) $F_t$ - Maximum photochemical yield as observed in dark adapted (-) $F^0_P$ -

### 2.5.1 Sustained non-photochemical quenching ($NPQ_s$)

Sustained non-photochemical quenching ($NPQ_s$) is a process that is relevant to plants that retain needles through the winter. This is another NPQ mechanism in addition to the reversible NPQ that we introduced in the previous section (Eq. **??**). In previous work with the Community Land Model (CLM) model(Raczka et al., 2019), a parameterization for sustained NPQ based on the state of acclimation was developed. We have already used state of acclimation in the photosynthesis model of QUINCY (Eq. **??**). Following the earlier work and similarly to the state of acclimation, we obtained for $K_{N_{sus}}$:

$$K_{N_{sus}} = \frac{K_{N_{sus,max}}}{1 + e^{b_{NPQ_s}(S - T_{NPQ_s})}}$$

where $b_{NPQ_s}$ ($°C^{-1}$) and $T_{NPQ_s}$ (°C) are parameters, set to 0.5 $°C^{-1}$ and 5.0 °C, respectively. The difference between this equation and Eq. (**??**) is that it has large values in winter, while Eq. (**??**) has large values during the summer. $S$ is obtained from Eq. (**??**). To parameterize the Eq. (7) we used SIF observations from US-NR1 and tuned the values to get the best match with our model, since the previous study by Raczka et al. (2019) had developed the parameterization for this site using active leaflevel observations from coniferous forest Hyytiälä in Finland. For the parameters $b_{NPQ_s}$ and $T_{NPQ_s}$ (Eq. 7) we obtained values of 0.5 $°C^{-1}$ and 5.0 °C, respectively. We tested different values and chose those that best fit the datacanopy that we used in this study. The first approach uses the mSCOPE model, which has been implemented in the QUINCY model. This approach is hyperspectral and considers the attenuation of the SIF signal within the leaf. The L2SM model is not implemented in QUINCY; rather it uses QUINCY's output. In our case, it utilizes two spectral regions. This approach considers the attenuation of the SIF signal within the leaf. The final approach is based on an empirical relationship and estimates the escape fraction using the fraction of absorbed PAR and leaf reflectance obtained from QUINCY. All approaches consider SIF emission to be a diffuse flux.

When both reversible and sustained NPQ were taken into account, $K_N$ was then a sum of them, as

$$K_N = K_{N_{rev}} + K_{N_{sus}}.$$

## 2.6 ~~Models for the radiative transfer of the SIF signal~~

### 2.5.1 mSCOPE

The mSCOPE model (Yang et al., 2017) is a further development of the widely used SCOPE model (van der Tol et al., 2009) that has been eventually implemented in SCOPE 2.0 (Yang et al., 2021). In mSCOPE, the canopy is allowed to have a heterogeneous vertical canopy structure, whereas in SCOPE it is assumed to be homogeneous. The QUINCY model has a vertically varying canopy structure, as explained in Section 2.4. Therefore, the use of mSCOPE was more suitable than SCOPE for coupling with QUINCY.

In mSCOPE, the model Fluspect (Vilfan et al., 2016) calculates leaf reflectance, transmittance and ~~chlorophyll fluorescence~~ChlF. The radiative transfer of mSCOPE is described by two SAIL-based models (Verhoef, 1984): one, which calculates the radiative transfer of incident radiation, and another one, which calculates the radiative transfer of emitted ~~chlorophyll fluorescence~~ChlF. Homogeneity in the horizontal direction is assumed, but heterogeneity of leaf properties in the vertical direction is allowed. The probability of sunlight on leaves is described by a Poisson model. The shaded leaves are illuminated only by diffuse radiation and their absorbed radiation does not depend on geometry. For the sunlit leaves, the absorbed radiation is calculated for discrete leaf orientations, including 13 leaf inclinations and 36 leaf azimuth angles relative to the solar azimuth. The soil optical properties are represented by a linear combination of a dry and a saturated soil reflectance factors, weighted as a function of the ratio soil moisture content to field capacity. The mSCOPE model calculates the top of the canopy (TOC) value for the ChlF emission.

The mSCOPE model has been implemented in QUINCY ~~. This implementation is now called QUINCY-mSCOPE, replacing~~ (see conceptual figure in Fig. S2). This implementation replaces the original QUINCY radiative transfer model (Spitters, 1986). The vertical profile of leaf chlorophyll, that was calculated inside QUINCY (S1.1), was used to calculate the radiative properties of each layer. ~~mSCOPE~~ To calculate this, mSCOPE uses the PROSPECT model (Jacquemoud and Baret, 1990) . mSCOPE runs over 60 canopy layers that were grouped to mimic the usual 10 layers in QUINCY as a function of the QUINCY layer LAI. mSCOPE outputs were then integrated for each layer group to represent each of the 10 QUINCY layers. For stability reasons, we also had to limit the calculation of the radiative transfer code to solar zenith angles below 80°. To test the implementation, we performed a sensitivity analysis by running simulations with different parameter values in both mSCOPE and QUINCY-mSCOPE. The results were consistent (not shown), so we are confident that there are no major technical errors in the implementation. Using ~~QUINCY-mSCOPE instead of QUINCY-orig~~ QUINCY with mSCOPE instead of QUINCY with the original radiative transfer model caused small differences in the simulated GPP, but overall the results were similar (for CA-Obs the Pearson correlation coefficient ($r^2$) was 0.99 for half-hourly values throughout the time period and the root mean squared error (RMSE) was 0.77 $\mu mol\, m^{-2}\, s^{-1}$). The viewing angle was set to nadir in ~~the QUINCY-mSCOPE~~ these simulations.

### 2.5.2 Layered two-stream model (L2SM)

The Layered canopy two-Stream Model (L2SM) (Knorr et al., 2025; Quaife, 2025) is a two-stream radiative transfer model based on the solutions provided by Meador and Weaver (1980)and . It allows the calculation of diffuse emissions originating from plant leaves. The total emission $E_{canopy}$ leaving the canopy, with the canopy including $L$ layers, is

$$E_{canopy} = \sum_{l=1}^{L} \frac{SIF_{leaf}}{2} \left[ \frac{T_{l-\frac{1}{2}}(1 + R_{L-l-\frac{1}{2}})}{1 - R_{l-\frac{1}{2}} R_{L-l-\frac{1}{2}}} \right]$$

where $R_{l-\frac{1}{2}}$ is the reflectance of the entire canopy above the middle layer $l$ A conceptual figure showing how it is used in combination with QUINCY is shown in Fig. S3, and $T_{l-\frac{1}{2}}$ is the transmittance of the same. $R_{L-l-\frac{1}{2}}$ is the reflectance of everything below the middle of layer $l$, including the soil. $\mathrm{SIF}_{\mathrm{leaf}}$ is the SIF emission from the layer, and in the formulation used here it is assumed to be equal in the upward and downward directions. The reflectance and transmittance of individual layers are combined using the technique of adding, so the combined reflectance $(R+)$ of two layers is given by

$$R_+ = R_1 + T_1^2 R_2 R_M$$

where $R_1$ is the reflectance of diffuse radiation from the upper layer, $T_1$ is the transmittance due to diffuse radiation of the upper layer and $R_2$ is the reflectance due to diffuse radiation from the lower layer (which could also be the soil). $R_M$ takes into account multiple diffuse reflections between layers and is given by

$$R_M = \frac{1}{1 - R_1 R_2}.$$

A detailed derivation and description of the equations of the model are in Section S1.5. The formulation of L2SM is a two-stream model, similar to the original radiative transfer model of QUINCY. Therefore it calculates the radiative transfer for the visible and near infrared region separately. Soil reflectance was assumed to be isotropic and leaf angle distribution was assumed hemispheric. We used L2SM can be found in Quaife (2025). As a starting point, we calculated the L2SM outside the QUINCY model. We gave the L2SM with the leaf reflectance (which also equals transmissivity in QUINCY), the leaf area index for each layer, and the SIF emission per layer (as calculated by Eq. **??**) .

The formulation of L2SM is a two-stream model, similar to the original radiative transfer model of QUINCY. However, while S15) as well as information on soil reflectance. In this implementation a novelty was that internal attenuation of the SIF signal was taken into account. While QUINCY is based on Spitters (1986), the L2SM approach is based on Meador and Weaver (1980). Therefore, the radiative transfer of incoming radiation used to calculate photosynthesis differs slightly from the way SIF is transferred within the canopy. A detailed derivation and description of the L2SM can be found in Quaife (2025)
.

An addition to earlier implementation of L2SM (e.g Knorr et al. (2025)) was that the attenuation of the SIF signal inside the leaf was taken into account. In this approach the leaf was split into two halves with equal optical depth and it was assumed that the SIF emission would originate from between those two layers. The doubling formula for optical media that has been illuminated by a diffuse flux at some certain wavelength gives for leaf reflectance a similar formulation as in Eq. (**??**). $T_{\frac{1}{2}}$ and $R_{\frac{1}{2}}$ are the transmittance and reflectance of the media split into two halves, following

$$T_{\frac{1}{2}} = \left(T(1 - R_{\frac{1}{2}}^2)\right)^{\frac{1}{2}},$$

and:

$$R_{\frac{1}{2}} = \frac{R}{1+T}.$$

When leaf spectra for $R$ and $T$ are given, an emission factor for an emitting factor $E_{leaf}$ for an emitting layer in the middle of a leaf can be calculated as:

$$E_{leaf} = \frac{T_{\frac{1}{2}}}{1 - R_{\frac{1}{2}}^2}.$$

This emission factor is used to calculate leaf-level SIF ($\mathrm{SIF_{leaf}}$) by:

$$SIF_{leaf} = E \times SIF_{internal}$$

where $\mathrm{SIF_{internal}}$ is the internal emission inside the leaf. For taking into account the wavelength, we used mathematically constructed estimate of the *in vivo* leaf spectrum, which was based on double Gaussian curve and normalized to one.

### 2.5.3 Liu and Zeng approaches (LZ)

In addition to modelling the transfer of the SIF signal, we have also tested some simpler formulations to estimate the SIF leaving the canopy. A more empirical approach was based on the work of Liu et al. (2020) (for the visible region) and Zeng et al. (2019) (for the near-infrared/far-red region). We used the formulation presented by Hao et al. (2021) for the escape fraction . The escape fraction describes how much of the emitted SIF signal reaches the top of the canopy. The total canopy SIF can be expressed using the escape fraction $f_{esc}$ as (Sun et al., 2017):

$$SIF = PAR \cdot fAPAR \cdot \Phi_{F_t} \cdot f_{esc}$$

where SIF is the observed SIF, PAR is the photosynthetically active radiation, fAPAR is the fraction of absorbed PAR and $\Phi_{F_t}$ is the chlorophyll fluorescence yield. (a conceptual figure is shown in Fig. S4). An empirically based formulation for the escape fraction $f_{esc}$ is:

$$f_{esc}^{reg} = \frac{\rho^{reg}}{fAPAR \cdot \sigma^{reg}} \frac{\rho_{can}^{reg}}{fAPAR \cdot \sigma^{reg}} \tag{3}$$

where reg is either visible (vis) or near-infrared (nir) region, $\rho$ $\rho_{can}$ is the reflectance of green vegetation and $\sigma$ is the single leaf scattering albedo, which is the sum of reflectance and transmittance. Therefore, this escape fraction is calculated separately for the visible and the near-infrared regions. The soil was assumed to be black, i.e. non-reflectant. To estimate the escape fraction from QUINCY in this way, we used the modelled vegetation reflectance for the whole canopy, fAPAR and the constants for single-leaf scattering albedoconstants. After calculating the escape fraction, the upscaled SIF emission (calculated as the sum of canopy layer SIF emissions from Eq. (??S15) which were multiplied by the canopy LAI) was multiplied by to obtain the estimate of the SIF signal.

### 2.5.4 Upscaling only

In order to estimate the importance of the escape factors for the different approaches and to see the influence of the different radiative transfer approaches, we also calculated the emission of the SIF signal with a simple upscaling of the simulated leaf level SIF, i.e., without any attenuation of the signal taking place within the canopy and assuming the escape factor then to be one. This approach was therefore integrating emission from all leaves. We calculated the upscaled signal for the red region only, using the leaf level SIF emission from Eq. (??). We summed the different layers of the SIF emission by multiplying each layer by its LAI value.

We did this to have a point of comparison with the other methods and to estimate the gain of the more computationally intensive approaches. We expected this method to give a large overestimation of the SIF signal at the top of the canopy, but we were interested to see if other methods showed superior performance, e.g. in terms of seasonality or diurnal cycle.

## 2.6 Converting the units of SIF from modelled to observed

The output of the radiative transfer approaches in Sections 2.5.2 ?? 2.5.1-2.5.3 is in flux units, i.e. $\mu\mathrm{mol\,m^{-2}\,s^{-1}}$. To be able to compare the model output with the observations, which are typically in units of $\mathrm{Wm^{-2}s^{-1}nm^{-1}sr^{-1}}$, we need to convert the units of the model output. This procedure was similar as described in Knorr et al. (2025). The Planck equation was

In the unit conversion, the Planck equation is used to obtain energy the energy $E$ of photons per mole . For the LZ and Upscaled approaches we used a spectrum observed at Hyytiälä Scots pine forest, located in central Finland (?) (Fig. 1), to weight the relative strength of the emissions at certain wavelengths compared to a reference SIF spectrum (for the L2SM

~~approach this was done already in leaf attenuation part, see Section 2.5.2).~~ as

$$E = \frac{N_a h c}{\lambda_\phi} \tag{4}$$

where $N_a$ is Avogadro's number (value is $6.022 \cdot 10^{23}$), $h$ is the Planck's constant ($6.626 \cdot 10^{-34}\ Js$), $c$ is the speed of light ($3.0 \cdot 10^8\ m\,s^{-1}$) and $\lambda_\phi$ is the wavelength of the SIF photons (unit $m$).

The emittance of SIF from the top of the canopy ~~was~~ is assumed to be isotropic, so the conversion to steradians ~~was~~ is done using a constant factor of $\frac{1}{\pi}$. The final step is to weight the relative strength of the emissions at wavelengths $\lambda_\phi$ compared to a reference SIF spectrum as:

$$w = \frac{e_s(\lambda_\phi)}{\sum_i e_s(\lambda_{\phi,i})}, \tag{5}$$

where $e_s$ is the emission spectrum in relative units. The emission was calculated for the wavelengths of the observing instruments (PhotoSpec or FloX). Similarly to Knorr et al. (2025), we used a spectrum observed at Hyytiälä Scots pine forest, located in central Finland (Magney et al., 2019a; Magney and Frankenberg, 2019) for the LZ approach. Observations of four trees were made at a light level of 1200 $\mu mol\,m^{-2}\,s^{-1}$ and these spectra were then averaged. For the L2SM we used mathematically constructed estimate of the *in vivo* leaf spectrum (Gordon, 1979), which was based on double Gaussian curve and normalized to one. This was done, since the current version of L2SM includes the leaf attenuation of the SIF signal.

Using this information, the unit conversion of the original SIF, $SIF_{unit,flux}$, to the SIF in measured units, $SIF_{unit,eng}$ is obtained as follows:

$$SIF_{unit,eng} = SIF_{unit,flux} \frac{e_{sw}}{\pi}. \tag{6}$$

The QUINCY run with mSCOPE provides fluorescence radiance units, and is therefore independent of this approach.

### 2.7 Sustained non-photochemical quenching ($NPQ_s$)

Sustained non-photochemical quenching ($NPQ_s$) is a process that is relevant to plants that retain needles through the winter. This is another NPQ mechanism in addition to the reversible NPQ that we introduced in the S1.4 section (Eq. S14). In previous work with the Community Land Model (CLM) model (Raczka et al., 2019), a parameterization for sustained NPQ based on the state of acclimation was developed. We have already used state of acclimation in the photosynthesis model of QUINCY (Eq. S5). Following the earlier work and similarly to the state of acclimation, we obtained for $K_{N_s}$:

### 2.8 ~~Modelling protocol~~

$$K_{N_s} = \frac{K_{N_{s,max}}}{1 + e^{b_{NPQ_s}(S - T_{NPQ_s})}} \tag{7}$$

where $K_{N_{s,max}}$, $b_{NPQ_s}$ ($°C^{-1}$) and $T_{NPQ_s}$ (°C) are parameters, set to 8.0, 0.5 $°C^{-1}$ and 5.0 °C, respectively. The difference between this equation and Eq. (S5) is that it has large values in winter, while Eq. (S5) has large values during the summer. $S$ is obtained from Eq. (S4). To estimate the parameters in the Eq. (7) we used SIF observations from US-NR1 and tuned the values to get the best match with our model considering the whole observational time period. The previous study by Raczka et al. (2019) had developed the parameterization for this site using active leaf level observations from coniferous forest Hyytiälä in Finland. We tested different values and chose those that best fit the data. A seasonal cycle of $K_{N_s}$ and and S at Sodankylä in 2021 are shown in Fig. S5.

When both reversible and sustained NPQ were taken into account, $K_N$ was then a sum of them, as

$$K_N = K_{N_{rev}} + K_{N_s}. \tag{8}$$

### 2.8 Site scale flux simulation protocol

All the sites of the study were classified as boreal coniferous evergreen forests PFT in QUINCY. Therefore also the soil reflectance was described similarly for all the sites. In this work we took advantage of the modular structure of QUINCY and used only the canopy model in our simulations. The LAI and leaf nitrogen content were prescribed so that the average summertime GPP level matched the observations. The meteorological forcing (air temperature, precipitation, atmospheric pressure, vapor pressure deficit, wind speed, short and longwave radiation) to run the model was obtained from the site measurements. In addition, we used atmospheric $CO_2$ concentration and N deposition, but the N cycle was not active in the canopy model simulations. The canopy model does not require any spinup and the simulations were performed for the years of the observations. The leaf single scattering albedo used to calculate reflectance for conifers was 0.15 in the visible wavelength region and 0.73 in the near infrared (Otto et al., 2014). The soil albedo for all the sites was estimated to be 0.15 in the visible and 0.30 in the near infrared. The LAI values have been set to lower values than observations, to make a better match with the observed magnitude of GPP. The LAI was set to 2.5 $m^2\,m^{-2}$ in CA-Obs, 3.6 $m^2\,m^{-2}$ in US-NR1 and 1.2 $m^2\,m^{-2}$ in FI-Sod. When presenting the results in Section 3.1, we had used the sustained NPQ presentation for the CA-Obs and US-NR1 sites, but not for the FI-Sod site.

### 2.9 Evaluation methodology

The metrics to assess the model performance were coefficient of correlation ($r^2$) (Wright, 1921), bias and root mean square error (RMSE) (Hastie et al., 2009) as well as its systematic and random components (Willmott, 1981). These formulas have been shown in Section S1.6.

For many of the figures we used averaging window of 15 days to smooth the daily values, so that the seasonal cycle would be easy to distinguish. Without satisfactory modelling performance of GPP, the simulation of the SIF would not be successful, as output from the photosynthesis model was used in our approach to calculate the leaf level emissions of SIF and this is why we also showed evaluation of GPP. We show for the subdaily time scale separately metrics for the model performance on morning

(6 a.m. to 9:30 a.m.), midday (10 a.m. to 1:30 p.m.) and afternoon (2 p.m. to 5:30 p.m). All of these times are local winter time.

Since the mSCOPE was run inside QUINCY and the two other approaches outside QUINCY, the wall time calculation differed. For the mSCOPE version the wall time was calculated as the time it took for QUINCY to simulate one year at FI-Sod. For the L2SM and the LZ approaches QUINCY was first run for one year at Sodankylä, and then the calculation outside QUINCY in Python was added to this wall time value.

# 3 Results

The diurnal monthly cycles and the seasonal cycles of the observed and simulated SIF signals for the years 2019 and 2020 at CA-Obs are shown in Fig. 2. This was the final result we obtained after testing for different radiative transfer schemes and adding the description for sustained NPQ. ~~In the following sections we~~ The following sections describe how we arrived at these results. In the main text~~we concentrate on~~ , we focus on the results from the CA-Obs site~~from~~ , for which we had ~~most data and show in the supplement~~the most data. In the supplement, we present the results for the other two sites.

## 3.1 Performance of the radiative transfer models

### 3.1.1 CA-Obs

The different radiative transfer schemes were all tested at all three sites. The monthly diurnal cycles and midday values (10 a.m. to 1:30 p.m.) for GPP, red region SIF and far-red SIF at CA-Obs ~~are shown in~~ (Fig. 3) showed large overestimation with all the different SIF transfer schemes. The midday values are shown here to give a better insight into how the magnitude of the variables changes, thus removing the strong influence of the change in day length on the results. ~~The forest in CA-Obs experienced a strong seasonal cycle with low levels of photosynthetic activity between October and March. The highest observed levels of photosynthesis and SIF occurred in July and August.~~ QUINCY was able to capture ~~this~~ the seasonal behaviour at the site. ~~In spring 2019 the eddy covariance observations were out of commission and until mid-2019 the GPP data was based on gap–filling.~~

~~All of the different SIF transfer schemes overestimated the magnitude of the observed SIF signals (Fig. 3). We decided not to plot the upscaled value in this figure, as its magnitude was much larger than from the other approaches.~~ The large overestimation of the SIF simulation results will be discussed also later in this paper. ~~The $r^2$ and RMSE values for the different methods for the daily means and different times of the day at CA-Obs are shown for SIF and GPP in Table 2 and the simulation results versus observations for the midday values are shown in Fig. 4 with the months marked in different colors.~~

~~Without satisfactory modelling performance of GPP, the simulation of the SIF would not be successful, as the photosynthesis model was used in our approach to calculate the leaf level emissions of SIF and this is why we also show evaluation of GPP.~~ The model performance of GPP in CA-Obs was generally good ~~. The $r^2$ between predicted and measured daily GPP was 0.88~~ (Table 2). The simulation of GPP was best at midday, and slightly less in morning hours. Since there was a long gap in observed

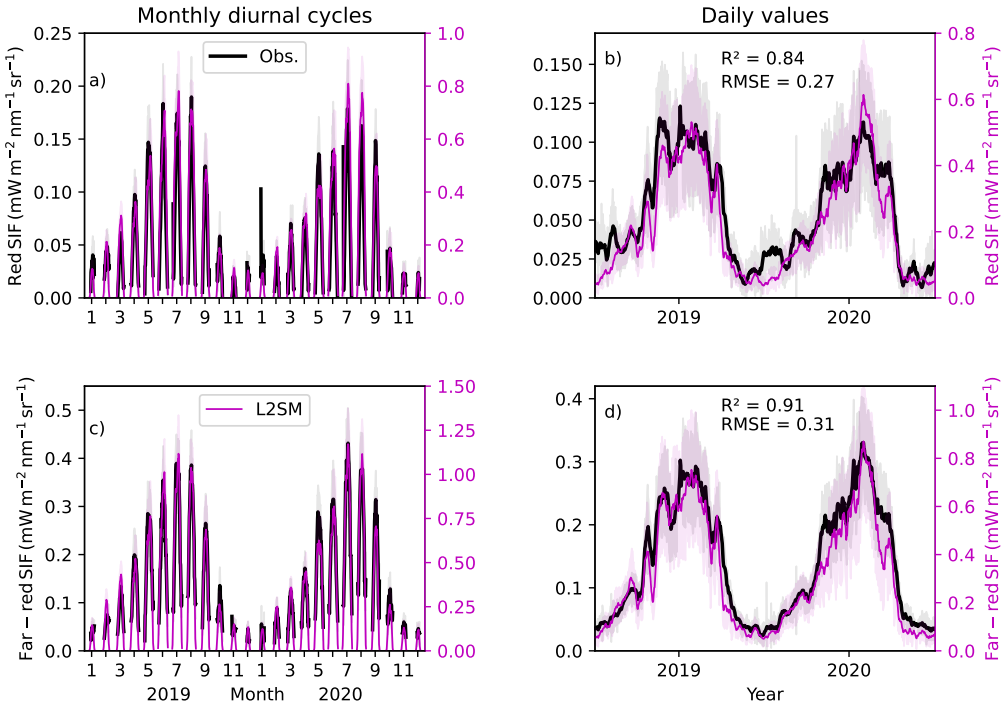


**Figure 2.** Monthly diurnal cycles for ~~red region SIF~~ (a) ~~and far-red~~ red region SIF and (c) far-red SIF and daily values for ~~red region SIF~~ (b) ~~and far-red~~ red region SIF and (d) far-red SIF at CA-Obs. The black line is the observation for all plots, magenta for the L2SM. All the lines for daily values have been smoothed with a 15-day long window. The shaded regions denote standard deviation. The metrics shown have been calculated from daily, non-smoothed values. The RMSE is in units $\mathrm{W m^{-2} s^{-1} nm^{-1} sr^{-1}}$.

GPP in and we instead used gap–filled GPP, we also checked the $r^2$ of daily GPP values for the two years separately. For 2019 the $r^2$ was 0.89 and for 2020 0.86, possibly reflecting the fact that simulations did not capture the turbulent nature of eddy covariance observations, but were potentially closer to gap–filled values that estimate the average behaviour of the ecosystem.

The daily $r^2$ values for SIF were close to those of GPP ~~, even slightly higher for the far-red region, which can be considered surprising, because modelling of SIF is based on modelling of GPP~~ (Table 2). Overall, ~~the modelling approaches for SIF were~~ modelling of SIF was more successful in the far-red region than in the red region. The $r^2$ values in both wavelength regions were better in the midday and afternoon than in the morning. ~~The lower performance in the morning could be due to sun-view geometry and the 3D structure of the canopy casting shades in the spectroradiometer measurement footprint that were not reproduced by the 1D radiative transfer models.~~ When investigating whether the different months showed clearly different

**Table 2.** The $r^2$ and RMSE values of simulated versus observed SIF values in the red and far-red regions in 2019-2020, according to different radiative transfer approaches at CA-Obs. The metrics are also shown for the GPP derived from the standard QUINCY configuration. The morning values are from 6 a.m. to 9:30 a.m., the midday values from 10 a.m. to 1:30 p.m., and the afternoon values from 2 p.m. to 5:30 p.m.

| Variable (unit) / $r^2$ (RMSE) | Daily | Morning | Midday | Afternoon |
|---|---|---|---|---|
| GPP ($\mu mol\,m^{-2}\,s^{-1}$) | 0.88 (1.47) | 0.83 (2.71) | 0.87 (2.19) | 0.84 (2.15) |
| Red region SIF ($Wm^{-2}s^{-1}nm^{-1}sr^{-1}$) | | | | |
| mSCOPE | 0.85 (0.21) | 0.68 (0.23) | 0.88 (0.29) | 0.82 (0.32) |
| L2SM | 0.84 (0.27) | 0.68 (0.27) | 0.86 (0.31) | 0.84 (0.34) |
| LZ | 0.83 (0.59) | 0.68 (0.54) | 0.86 (0.66) | 0.83 (0.72) |
| Upscaled | 0.84 (1.45) | 0.68 (1.34) | 0.88 (1.89) | 0.84 (1.70) |
| Far-red region SIF ($Wm^{-2}s^{-1}nm^{-1}sr^{-1}$) | | | | |
| mSCOPE | 0.92 (0.18) | 0.87 (0.21) | 0.91 (0.27) | 0.89 (0.28) |
| L2SM | 0.91 (0.31) | 0.87 (0.31) | 0.90 (0.38) | 0.92 (0.38) |
| LZ | 0.91 (1.20) | 0.87 (1.13) | 0.90 (1.49) | 0.92 (1.43) |

patterns in model behaviour (Fig. 4), it was seen that the highest simulated midday values in summer were higher than the linear fit between observations and simulations would imply, suggesting that the model had a tendency to overestimate these values relative to other time periods. ~~The relationship between observed and simulated values appeared to be more curvilinear in the far-red than the red, with some generally lower values simulated for the observation between 0.3 and 0.5 .~~

The performance of the different modelling approaches was quite comparable when looking at the $r^2$ values (Table 2). The RMSE values showed greater variation~~, but due to the large overestimation by all the models, it is probably not useful to use this as a metric to evaluate the model performance. The upscaled value, which did not include any signal attenuation, performed at a comparable level to more sophisticated approaches if only $r^2$ is considered.~~ . Of the three different radiative transfer approaches, L2SM appeared to have a consistent level of performance in both wavelength ranges and different times of the day. Overall, the $r^2$ values were quite similar between the approaches, showing that the different approaches did not have a pronounced influence on the temporal patterns of the simulated SIF.

### 3.1.2 US-NR1 and FI-Sod

Running the same simulations at other sites allowed further evaluation of model performance and possible influences of instrumentation on the diurnal dynamics. ~~For the US-NR1 results we used the same parameterization for sustained NPQ as for CA-Obs. For the FI-Sod we did not include sustained NPQ. We discuss this further in Section 3.2.~~

~~At US-NR1, measurements were available from June 2017 to early June 2018. US-NR1 is at a lower latitude than the other study sites, but the high elevation conditions result in a pronounced seasonal cycle with seasonally below freezing winters.~~

~~The forest is photosynthetically active from May to September, with the shoulder season to winter occurring in October and December, and spring recovery occurring in April and May (Fig. S1).~~

The model performance for simulating GPP and SIF was lower in US-NR1 than in CA-Obs (~~$r^2$ for daily values was 0.80, Table S1~~Table S2, Fig. ~~S1). The $r^2$ values of the different SIF simulations were much lower in US-NR1 than in CA-Obs (Table S1). This~~ S6). For SIF this is clearly seen in the amount of scatter between simulated and observed values in Fig. ~~S2~~S7. The model seemed to have difficulty in capturing the variation in midday values during the summer months. The seasonal cycle of SIF in US-NR1 was not as well reproduced as in CA-Obs (Fig. ~~S3b~~ S6b vs. Fig. 5b), although the spring recovery of GPP seemed to be well simulated (Fig. ~~S1b).~~

S5b). Similar to CA-Obs, the $r^2$ values for SIF were generally higher in the far-red region than in the red region at US-NR1 (Table ~~S1~~S2). The model performance was best at midday. ~~The comparison between the different radiative transfer approaches showed that the upscaled value without any described radiative transfer had the highest $r^2$ values in the red region, and mSCOPE in the far-red region.~~

~~FI-Sod is located 100 km north of the Arctic Circle, so winter radiation is zero and temperatures are low. Spring recovery occurs in April and May, the photosynthetically active period is from June to August and photosynthesis ceases in September and October (Fig. S4).~~ QUINCY was more successful in simulating GPP at FI-Sod than at the other two sites (~~Table S2~~Fig. S8, Table S3). Modelling SIF was less successful than modelling of GPP in FI-Sod (Table ~~S2~~S3, Fig. ~~S5~~S9). In both spectral regions, the model performed best in the morning and midday, and worse in the afternoon. Differences between the radiative transfer approaches were not pronounced.

### 3.1.3 Comparison performance between sites and computational efficiency

The magnitude of the observed SIF was similar in both the red and far-red regions at the two sites with the PhotoSpec observations (Table ~~S3~~S4) for the July-August midday values. Compared to these values, the FI-Sod value observed with FloX was higher in the red region and lower in the far-red region, which was consistent with what we see in the spectral shape of the SIF emission (Fig. 1). In the far-red region this difference was more pronounced and was half of the value observed with PhotoSpec (Table ~~S3~~S4). The overestimation of SIF by the different radiative transfer methods was most pronounced for the sites with PhotoSpec observations in the red region. In the far-red region, mSCOPE had the lowest overestimation~~and LZ approach~~ , while the LZ approach had the highest.

~~The escape fraction was calculated as a fraction of the averaged simulated midday SIF value in July-August and the corresponding upscaled value. The results were around 0.2 in the red region, with some higher values with the LZ approach (Table **??**). In the far-red region there was more variation between the estimated escape fractions. Generally the escape ratios were lower in the red region compared to the far-red, which was what would be expected. mSCOPE predicted the lowest values of the approaches in the far-red. As the differences in performance of mSCOPE and~~ The same was true when looking at the metrics for all the sites combined (Table 3. The LZ approach had the highest bias and systematic RMSE across the sites. Otherwise, generally mSCOPE had the best performance metrics, but the other approaches were not much worse. In the North American sites the model approaches performed better in the far red region.

As the simulation time is relevant for large scale applications, we calculated wall times for the simulations for one year at FI-Sod (Table 4). LZ was 419 times faster than the mSCOPE approach, while L2SM ~~radiative transfer approaches were quite similar, the remainder of the analysis is mainly based on the use of the L2SM, as it was computationally efficient to run~~took twice as long as LZ while being 210 times faster then the mSCOPE approach.

### 3.2 Importance and generality of sustained NPQ modelling

SIF modelled without sustained NPQ showed a strong relationship with the absorbed PAR (aPAR) at CA-Obs (Fig. 5a). A CA-Obs simulation was carried out to assess the performance of the parameterization carried out at US-NR1. QUINCY was successful in simulating the aPAR at CA-Obs at midday (Fig. 5a, Table 5). The seasonal cycle was strong with winter values of aPAR around 200 $\mu\mathrm{mol\,photons\,m^{-2}\,s^{-1}}$. The increase towards summer values in aPAR started earlier than ~~the ecosystem response~~for the observed GPP, as the low temperatures prevented the spring recovery of vegetation. The increase towards summer values of aPAR started already in the first part of the year, much earlier than the SIF values started to increase strongly (Fig. 5). The simulated SIF without the described $\mathrm{NPQ_s}$ followed the behaviour of the absorbed PAR. The simulated SIF with the $\mathrm{NPQ_s}$ was more similar to the observed seasonal behaviour (Fig. 5b, Table 5). The magnitudes between the simulations and observations differed for SIF, but the general timing was better for the simulation with $\mathrm{NPQ_s}$. The $\mathrm{NPQ_s}$ had a strong influence on the chlorophyll fluorescence yield ($\Phi_F$) in the model (Fig. 5c). ~~There was no feedback from the modelling of SIF back to the photosynthesis part of the QUINCY model currently, so describing the $\mathrm{NPQ_s}$ did not influence modelling of GPP. However, similar mechanism based on state of acclimation as used in $\mathrm{NPQ_s}$ has been implemented for spring recovery of GPP in the QUINCY model already earlier.~~

As US-NR1 is more southerly than CA-Obs, the absorbed PAR did not show a pronounced seasonal cycle (Fig. ~~S3a). This was reflected in the simulated SIF , so that the simulation~~ S10a). The simulated SIF without $\mathrm{NPQ_s}$ ~~showed no clear seasonal cycle . Using the formulation for~~ followed the seasonal cycle of absorbed PAR. In order to simulate the seasonal variation seen in the SIF observations, it was necessary to include $\mathrm{NPQ_s}$ ~~gave the simulated SIF a seasonal cycle, but the formulation used~~ in the modelling. However, the formulation used for $\mathrm{NPQ_s}$ delayed the spring recovery in 2018 too much. The formulated $\mathrm{NPQ_s}$ also slightly affected the summer time values, which is physiologically unlikely to happen in reality. Inclusion of $\mathrm{NPQ_s}$ improved the simulations results considerably in terms of $r^2$, RMSE and bias.

As FI-Sod is located north of the Arctic Circle and the absorbed PAR had a pronounced seasonal cycle (Fig. ~~S6a~~S11a). The ~~colder air temperatures caused the $\Phi_F$ to drop to a lower level than at the other two sites (Fig. S6b). However, even with this decrease, the~~ absorbed PAR caused the simulated SIF values to start to increase already in February, well before the start of the vegetation active period ~~.~~(Fig. S11). There were no tower flux SIF observations at the site at that time, but it is not likely that the SIF would have increased considerably so early. Therefore, it seems that the same parameterization that gave reasonably satisfactory results at the other two sites was not as functional at this more northern site with different climatic characteristics (Fig. ~~S6b).~~ S11b). The aPAR observed by the above- and belowground canopy PAR sensors showed much better resemblance to simulations than the aPAR estimated from the FloX measurements (Table 5). This suggests that the shadow effects in the footprint of the FloX observations likely influence the observation and in a way set the limit to which model simulations can

**Table 3.** ~~Escape fractions for~~ The $r^2$, bias, $RMSE_{sys}$ and $RMSE_{ran}$ values of simulated versus observed SIF values in the red and far-red regions according to different radiative transfer approaches ~~calculated for July-August midday values (10 a.m. to 1:30 p.m) as a fraction of~~ at the ~~upscaled value for the~~ three sites. The metrics are also shown for the GPP derived from the standard QUINCY configuration. The values are calculated on daily values.

| ~~$f_{esc}$~~ Variable (unit) | ~~CA-Obs~~ $r^2$ | ~~US-NR1~~ Bias | ~~FI-Sod~~ $RMSE_{sys}$ | $RMSE_{sys}$ |
|---|---|---|---|---|
| CA-Obs: Red region SIF ($Wm^{-2}s^{-1}nm^{-1}sr^{-1}$) | | | | |
| mSCOPE | ~~0.19~~ 0.85 | ~~0.17~~ 0.15 | 0.21 | 0.01 |
| L2SM | ~~0.20~~ 0.84 | ~~0.16~~ 0.21 | ~~0.26~~ 0.27 | 0.02 |
| LZ | ~~0.37~~ 0.83 | ~~0.33~~ 0.47 | ~~0.52~~ 0.59 | 0.02 |
| CA-Obs: Far-red region SIF ($Wm^{-2}s^{-1}nm^{-1}sr^{-1}$) | | | | |
| mSCOPE | ~~0.25~~ 0.92 | 0.12 | 0.18 | 0.03 |
| L2SM | 0.91 | 0.24 | ~~0.17~~ 0.31 | 0.03 |
| LZ | 0.91 | 0.95 | 1.20 | 0.03 |
| US-NR1: Red region SIF ($Wm^{-2}s^{-1}nm^{-1}sr^{-1}$) | | | | |
| mSCOPE | 0.67 | 0.25 | 0.29 | 0.02 |
| L2SM | ~~0.30~~ 0.62 | ~~0.26~~ 0.27 | ~~0.24~~ 0.30 | 0.03 |
| LZ | ~~0.85~~ 0.63 | ~~0.75~~ 0.60 | 0.67 | 0.03 |
| US-NR1: Far-red region SIF ($Wm^{-2}s^{-1}nm^{-1}sr^{-1}$) | | | | |
| mSCOPE | 0.74 | 0.25 | 0.28 | 0.06 |
| L2SM | 0.70 | 0.33 | 0.36 | 0.07 |
| LZ | 0.73 | 1.23 | 1.36 | 0.06 |
| FI-Sod: Red region SIF ($Wm^{-2}s^{-1}nm^{-1}sr^{-1}$) | | | | |
| mSCOPE | 0.65 | 0.14 | 0.15 | 0.04 |
| L2SM | 0.58 | 0.33 | 0.35 | 0.04 |
| LZ | 0.57 | 0.81 | 0.86 | 0.04 |
| FI-Sod: Far-red region SIF ($Wm^{-2}s^{-1}nm^{-1}sr^{-1}$) | | | | |
| mSCOPE | 0.65 | 0.20 | 0.21 | 0.03 |
| L2SM | 0.59 | 0.34 | 0.36 | 0.04 |
| LZ | 0.59 | 1.25 | 1.32 | 0.04 |

be successful. The temperature response of the chlorophyll fluorescence yield ($\Phi_F$) showed further the pronounced difference depending on whether the $NPQ_s$ was included or not (Fig. S12). There were no differences between the sites. Temperature

**Table 4.** Wall times in seconds for different radiative transfer approaches.

| | mSCOPE | L2SM | LZ |
|---|---|---|---|
| Wall time (seconds) | 4191 | 20 | 10 |

**Table 5.** The metrics ($r^2$, RMSE and bias) of the simulated absorbed PAR (aPAR) and far-red region (FR) SIF at the three sites for midday values with and without the formulation for $NPQ_s$. The units of RMSE and bias are $\mathrm{Wm^{-2}s^{-1}nm^{-1}sr^{-1}}$ for far red region SIF and $\mu\mathrm{mol\,m^{-2}\,s^{-1}}$ for APAR.

| Site and variable | $r^2$ | RMSE | Bias |
|---|---|---|---|
| CA-Obs | | | |
| aPAR | 0.94 | 91.6 | 13.4 |
| FR SIF, no $NPQ_s$ | 0.71 | 0.59 | 0.51 |
| FR SIF, with $NPQ_s$ | 0.90 | 0.43 | 0.32 |
| US-NR1 | | | |
| aPAR | 0.83 | 256.1 | 205.3 |
| FR SIF, no $NPQ_s$ | 0.24 | 0.76 | 0.72 |
| FR SIF, with $NPQ_s$ | 0.71 | 0.42 | 0.37 |
| FI-Sod | | | |
| aPAR (FloX) | 0.70 | 159.9 | 71.4 |
| aPAR (PAR sensors) | 0.96 | 73.9 | -13.2 |
| FR SIF, no $NPQ_s$ | 0.70 | 0.31 | 0.23 |
| FR SIF, with $NPQ_s$ | 0.69 | 0.28 | 0.18 |

response of the ratio daily far-red SIF divided by GPP showed that the ratio increased in cold temperatures at the North American sites in both the observations and simulations (Fig. S13). The simulated values showed much larger SIF:GPP values than the observations. Observations at FI-Sod did not cover enough wide range in temperature to show such a variation.

### 3.3 Dependencies between far-red SIF, GPP and PAR

Noticeable differences were found comparing the relationship between GPP and far-red SIF in the observations and simulations with L2SM for June and July (Fig. 6). The observations presented equally high far-red SIF values for CA-Obs and US-NR1, although the observed GPP values were higher at CA-Obs (Fig. 6a). Both observed GPP and far-red SIF values were lower at FI-Sod compared to the North American sites (Fig. 6a). ~~At FI-Sod the instrument measuring SIF was different and far-red SIF retrieved at different wavelengths. Overall, the observed GPP values featured high variability for simultaneous SIF~~

**Table 6.** Model performance in terms of $r^2$ and RMSE for GPP and SIF in the far-red region at three sites for half-hourly values during five summer days and the averaged diurnal cycle over the five days. Calculated for half-hourly values at CA-Obs and hourly values at US-NR1 and FI-Sod. RMSE for GPP is in units $\mu mol\,m^{-2}\,s^{-1}$ and for SIF in $Wm^{-2}s^{-1}nm^{-1}sr^{-1}$.

| | CA-Obs | US-NR1 | FI-Sod |
|---|---|---|---|
| GPP, $r^2$ (RMSE) | | | |
| half-hourly | 0.60 (3.42) | 0.26 (2.77) | 0.98 (0.59) |
| averaged | 0.80 (2.08) | 0.51 (1.79) | 0.99 ~~GPP, RMSE (~~(0.50) |
| ~~half-hourly 3.42 2.77 0.59 averaged 2.08 1.79 0.50~~ SIF, $r^2$ | | | |
| half-hourly | 0.69 (0.57) | 0.29 (0.52) | 0.40 (0.54) |
| averaged | 0.83 (0.51) | 0.66 (0.46) | 0.50 ~~SIF, RMSE (~~(0.53) |
| ~~half-hourly 0.57 0.52 0.54 averaged 0.51 0.46 0.53~~ height | | | |

~~observations. The observations did not show clear differences in the far-red SIF-GPP relationship between the morning and the afternoon values. The~~ The simulated values showed much less scatter for the SIF-GPP relationship than the observations (Fig. 6b). The highest far-red SIF values were obtained at CA-Obs, although the highest GPP values were obtained at US-NR1. ~~Some of the afternoon values were at a lower level than the morning values, this was seen especially for the CA-Obs simulation results.~~ When looking at the GPP and far-red SIF light responses (Fig. 7 e, g) it was noticed that the simulated far-red SIF values were highly correlated with the PAR values, while simulated GPP values had more scatter. ~~This was caused by the stomatal conductance lowering the GPP and it seems that this variation did not get reflected to simulated far-red SIF values.~~

We made a hyperbolic fit to these relationships, fitting parameters $a$ and $b$ of function y=ax/(b+x) (Damm et al., 2015; Pierrat et al., 2022b). The fitted lines are shown in Fig. 6 and the fitted parameter values with their associated uncertainties are shown in Table ~~S4. The simulated values had generally smaller uncertainties for the fitted parameter $a$, demonstrating the curvilinear relationship between the variables in the simulations that was not as pronounced in the observations, which can be partly be contributed to the high variability in the observations. However, for FI-Sod the small parameter $b$ value in fit to observations (Fig. 6b) leading to a strong curvature in the fitted curve also shows that~~ S5. Goodness of the hyperbolic fits (Table S5) were better for the simulated GPP vs. SIF relationship than for the observed (averaged over three sites $r^2$= 0.73 for the simulated, $r^2$=0.45 for the observed.) Also the RMSE of the fit was smaller for the simulations vs. observations for all the three sites. The worst behaviour of fits (in terms of $r^2$) happened at FI-Sod ~~results this relationship is quite linear~~ for the observations, potentially reflecting the fact that the GPP vs. SIF relationship looks quite linear for that site.

Given the worse model performance for SIF at US-NR1, the diurnal cycle during the summer was examined in more detail for all three sites. First, we calculated the $r^2$ and RMSE values for the instantaneous values over five days versus the averaged diurnal cycle over five days. The improvement in $r^2$ and RMSE when moving from instantaneous to averaged values was considerable (Table 6).

The $r^2$ values of the averaged diurnal cycle were comparable for GPP and SIF in the far-red region at CA-Obs (Table ~~7~~6). On day of year (DOY) 187, the simulated GPP showed an almost sinusoidal diurnal behaviour, which resulted from simulation under high irradiance conditions (Fig. 7a). The observed GPP showed more variation than simulated GPP during the day~~, which was maybe due to the canopy shading, the role of understorey vegetation and turbulence conditions~~. The light response of the observed GPP was much more scattered than that of the simulations (Fig. 7e). The simulated far-red SIF values with all the approaches were able to capture variations quite successfully on DOY 189 (Fig. 7c), when variations in radiation occurred.

At US-NR1 the model performance remained significantly lower for GPP than at the other two sites (Table 6) even after calculating the average over five days. The light response curves of the observed GPP and SIF in the far-red region were quite scattered at this site (Fig. ~~S7e~~S14e, f). The model performed very well for GPP at Sodankylä (Table 6, Fig. ~~S8~~S15). The modelled diurnal cycle of far-red SIF did not capture the variation in the observations (Fig. S8c, d). ~~The footprint of the FloX might be partially shadowed during some time periods in sunny days, causing mismatches between the observed and simulated far-red SIF (Fig. S8c,d). This might partly explain the lower model performance in the afternoon (Table S2), as the shadow effects might become larger in the shoulder seasons at a high latitude site. Designing an observation without shadow effects would be very challenging at such high latitudes with very long days during summer.~~

### 3.4 ~~Use~~ Comparison of simulated SIF to satellite observations~~in model development~~

The magnitude of the simulated SIF was large compared to the tower-based observations at all sites (Figs. 3, ~~S1, S4~~S6, S8). Comparison with satellite observations at CA-Obs showed a better agreement between the simulated and observed magnitudes (Fig. 8c) than proximal sensing (Fig. 8b). In 2019, the seasonal cycle of TROPOSIF was smoother than that of the simulated SIF and PhotoSpec observations at the site~~, reflecting the fact that satellites have a limited capacity to detect rapid phenological changes given the spatial and temporal averaging (Fig. 8b). Also, the cloudy days were filtered out from the TROPOSIF, while these were included in the in situ observations, a fact that further smoothed the satellite observations.~~ . In 2020, the seasonal cycle was smoother in the PhotoSpec observations and the simulated seasonal cycle was more consistent with TROPOSIF. The simulation results and the TROPOSIF are shown on different scales because the magnitude of the winter TROPOSIF observations is below zero due to the retrieval method, but the minimum of the simulated SIF is zero and using different scales helps to see the seasonality of the two observations together.

~~The mean daily value with standard deviation for the TROPOSIF at CA-Obs for the~~ The simulations for the period July-August ~~was 0.80 $\pm$ 0.24 . The simulations for this time period overestimated the value~~ overestimated the observations by 30 %. ~~At the~~

At FI-Sod ~~site, both the TROPOSIF product and simulations gave lower values than at CA-Obs. The TROPOSIF estimate~~ (Fig. S16) the TROPOSIF time series expanded also to spring, thus covering also for the period not available from the FloX observations. There was a lot of variation in the springtime TROPOSIF observations (shaded region in Fig. S16, from April 9th to May 17th) and when the values started to increase for the last time in May (the vertical line in Fig. S16 showing May 29th) the observed GPP was already at higher level than in early spring. The variation in TROPOSIF and simulated SIF during summer

**Table 7.** The metrics ($r^2$, RMSE and bias) of the simulated SIF at CA-Obs and FI-Sod against the TROPOSIF observations. The simulated values have been calculated from the midday values and TROPOSIF values are daily averages. The values are separately region around the site expanding to 0.50° x 0.50° or 0.25° x 0.25°. The units of RMSE and bias are $\mathrm{Wm^{-2}s^{-1}nm^{-1}sr^{-1}}$.

| Site and region | $r^2$ | RMSE | Bias |
|---|---|---|---|
| CA-Obs (0.50° x 0.50°) | 0.48 | 0.57 | 0.45 |
| CA-Obs (0.25° x 0.25°) | 0.46 | 0.64 | 0.55 |
| FI-Sod (0.50° x 0.50°) | 0.15 | 0.61 | 0.51 |
| FI-Sod (0.25° x 0.25°) | 0.26 | 0.64 | 0.58 |

followed the same pattern. Overestimation of the simulations compared to TROPOSIF observations for the July-August period was ~~0.60 ± 0.24 , which the simulations overestimated by~~ 45 %. ~~The values of TROPOSIF were significantly higher for~~

The performance metrics for simulated SIF against TROPOSIF were better at CA-Obs than ~~for~~ at FI-Sod ~~, by 33 %. This reflects the difference in GPP observations. The midday GPP at CA-Obs was on average 63 % higher than~~ (Table 7. This was partly contributed to the fact that the sustained non-photochemical quenching was not simulated at FI-Sod. The FloX observations alone were not sufficient to assess that, as the spring was missing from those, but one can see from the Fig. S16, that the increase should start later than it started here. Despite the large differences in the springtime at FI-Sod~~,~~ , the RMSE and bias were quite similar at the two sites for the larger region (having 0.50° x 0.50° region around the region). When constraining to a smaller region, RMSE and bias got worse for both of the sites, but the $r^2$ increased at FI-Sod, even though it was still quite small.

## 4 Discussion

### 4.1 ~~On the choice~~ Magnitude of ~~radiative transfer approach~~the simulated SIF

~~We first tested different ways of describing the radiative transfer of the SIF to decide which method would be robust enough for feasible calculations in a large-scale model . In general, all different methods greatly overestimated the magnitude of~~ All of the ~~in situ observations by a factor of many (Table S3), making it difficult to use the magnitude as a metric to judge modelbehaviour.~~ approaches that we tested overestimated the in situ observed SIF considerably (Table S4). The differences were less pronounced in the comparison against the satellite observations. The leaf level model was consistent across all our approaches. In that model, we used only the default parameters, which were held constant across all sites. The leaf level model provided the chlorophyll fluorescence yield, which was applied differently by each approach to obtain the top of canopy value.

Therefore, the reason for the overestimation of the SIF could originate from either the leaf level model or the radiative transfer calculation. The leaf level model provided the Ft, which was consistent with values in the literature (e.g., the original model formulation, (van der Tol et al., 2014); another modelling study for US-NR1 (Raczka et al., 2019); and site level observations

(Kim et al., 2021)). However, there are other types of estimates for these values, including some of these sites. For example, Pierrat et al. (2024) provide a higher leaf level chlorophyll fluorescence yield value from MoniPAM observations. In any case, the magnitude is subject to choices made in the post-processing of the data, so it is also not easy to compare the simulated value to these observations.

It is likely that the overestimation originated from the radiative transfer part of the model. Despite testing different approaches, they all led to overestimated SIF. Two approaches that included attenuation of the SIF signal inside the leaf (mSCOPE and L2SM) resulted in smaller overestimation than the approach that did not account for attenuation (LZ). Additionally, the version of the LZ approach employed here assumed black, or non-reflective, soil. Some recent developments may help overcome this issue (Yang et al., 2025a). The simulated far-red region SIF showed lower overestimation than the simulated red region SIF. This model behaviour suggests issues with attenuation in the red region. The modelling of SIF is also related to the modelling of absorbed PAR. At US-NR1, the simulations overestimated absorbed PAR, whereas at the other two sites, the bias in aPAR was smaller (Table 5. It has been noted, that parameters related to aPAR are important for SIF modelling (Fan et al., 2025).

The overestimation of SIF in evergreen conifer forests has also occurred in other modelling studies (Li et al., 2022), and our results are close to the model average ~~compared to~~ shown in a model comparison study conducted at US-NR1 (Parazoo et al., 2020). ~~Our comparison with the satellite observations showed that the discrepancy was not as pronounced as in the site-level observations . It may therefore~~ Preliminary model tests with QUINCY on other ecosystems did not reveal such significant discrepancies between the magnitude of the simulation results and in situ observations (results not shown). Therefore, it may be that the characteristics of the in situ sampling in this type of ecosystem to provide smaller SIF signals than expected. ~~Satellite observations also have a larger footprint that would in CA-Obs also include larch forests. Also, as the in situ observations were tower-based, it is possible that part of the observation footprint contained bare soil at FI-Sod site, which will hence have a lower SIF value, but our model only simulates one plant functional type per site and is horizontally homogeneous. In reality also the directional effects and shadows influence the observed optical signal (Hilker et al., 2008b, a). The PhotoSpec retrievals were filtered by having an Normalized Difference Vegetation Index (NDVI) based threshold to ensure that only observations of vegetation were used. Preliminary model tests on other ecosystems did not show such large discrepancies between the simulation results and in situ observations (results not shown). The satellite observations exploit also different wavelengths than the tower observations for SIF retrieval, which may~~ A comparison to satellite observations did not reveal such a large overestimation of the simulated SIF. One can keep in mind that also other processes may also play a role~~in how large the difference is between the observations and simulation results. As we only studied here the satellite observations at two sites, no conclusions can be drawn about how they generally relate to e.g. site level observations~~, such as reversible NPQ. The leaf level model that we used has been parameterized for cotton (van der Tol et al., 2014). (Raczka et al., 2019) used leaf level MoniPAM observations from Hyytiälä to parameterize reversible NPQ and improved the performance of their SIF model. This could be a way to improve modelling for new ecosystems.

### 4.2 On the choice of radiative transfer approach

~~Overall, when~~ First, we tested different ways of describing the radiative transfer of the SIF to determine a robust method for feasible calculations in a large-scale model. When considering the $r^2$ metric for the different approaches, ~~it was found that simple upscaling of the signal~~ we found that the simple LZ method did not perform significantly worse than the more sophisticated approaches (Tables 2, ~~S1,~~ S2, S3). This justifies the rather simple approaches previously used in the radiative transfer of SIF (e.g., Lee et al., 2015; Thum et al., 2017), but ~~is in contrast to~~ it contrasts with some other studies (Li et al., 2022). The mSCOPE model performed ~~as well as~~ similarly to the other approaches across all sites and often ~~gave best estimates, but~~ provided the most accurate estimates. However, its longer computation time (20 times longer than the other approaches in our comparison) makes it impractical for ~~use in~~ large scale applications (Li et al., 2022). The radiative transfer model in mSCOPE is based on SAIL, which was originally developed for croplands (van der Tol et al., 2009). The radiative transfer model in QUINCY was also originally developed for ~~crops~~croplands, so neither model was designed to consider the unique characteristics of radiative transfer in the conifer forests. A study by Li et al. (2022) found ~~a significant improvement in modeling SIF with CLM when they included~~ that including clumping in their model ~~in a simple manner compared to simulations without clumpingincluded. Not considering~~ significantly improved SIF modeling in CLM compared to simulation without clumping. Failing to consider clumping can lead to significant errors in SIF modelling (Zeng et al., 2020). QUINCY ~~has clumping described in a~~ describes clumping in a relatively simple way. There is potentially room for improvement in SIF modelling if clumping ~~is described more rigorously. The challenge in conifer ecosystems~~ were also included in the radiative transfer of SIF, e.g. in L2SM. In conifer ecosystems, the challenge is that the clumping of the canopy exposes more ground vegetation visible to optical measurements~~and therefore also~~ , which affects the remotely sensed signal (Gopalakrishnan et al., 2023).

The structure of the vegetation affects the observed SIF signal (Magney et al., 2019b; Sun et al., 2023a). This is something that could be addressed by including vegetation NIRv, a near-infrared reflectance~~that~~ , in the analysis. NIRv has very similar interactions within the canopy to the far-red region SIF. Including NIRv ~~, which can be used to approximate the escape ratio,~~ in helping to interpret the SIF signal in the analysis would allow the attribution of the structural effects seen in the SIF signal (Zeng et al., 2019; Dechant et al., 2022). This analysis could be conducted using in situ or spaceborne observations. Another approach would be to ~~account for~~ consider the 3D structure of the canopy in QUINCY and the SIF RT model. ~~In this way, the GPP and SIF would both be modulated in a consistent way (Stretton et al., 2025)~~This would allow for consistent modulation of both the GPP and SIF (Stretton et al., 2025).

### 4.3 Modelling performance of GPP and SIF at subdaily scale

Compared to the simulated GPP, the observed GPP showed more variation on a subdaily scale at the sites (Figs. 7, S14, S15). This variation may be due to canopy shading, understorey vegetation and turbulence conditions. The lower performance at CA-Obs in the morning may be due to sun-view geometry and the 3D structure of the canopy, which casts shadows within the spectroradiometer's measurement footprint. These shadows were not reproduced by 1D radiative transfer models.

At FI-Sod, the FloX footprint might be partially shadowed during certain periods on sunny days, resulting in discrepancies between the observed and simulated far-red SIF (Fig. S15c,d). This may partly explain the lower model performance observed

in the afternoon (Table S3), as the shadow effects may be more pronounced during the shoulder seasons at a high latitude sites. Designing an observation that excludes shadow effects would be very challenging at such high latitudes, where the days are very long days in the summer.

### 4.4 On the use of optical properties

Although L2SM supports vertically varying optical properties, ~~but in this work it has been set~~ this study set it up with properties that remain unchanged ~~through~~ throughout the canopy profile. However, the vertical profile of leaf chlorophyll content could be used to ~~redefine~~ adjust the optical properties of each layer. In the current version of QUINCY, the chlorophyll content ~~of canopy layers~~ increases with depth within canopy layers. The single leaf scattering albedo of forest plant functional types in QUINCY is based on a study by Otto et al. (2014). ~~The values~~ Values commonly used to calculate reflectance and transmittance in terrestrial biosphere models have been criticized, and some new approaches based on more data have been proposed (Majasalmi and Bright, 2019). ~~Reflectance~~ Since reflectance was also used in the calculation of the LZ approach ~~, so~~ calculation, it would also influence these results ~~. Also the assumption of having~~ as well. The assumption of equal reflectance and transmittance in QUINCY can be ~~argued (Majasalmi and Bright, 2019)~~ debated and further developed~~. Also the~~ , as discussed in Majasalmi and Bright (2019). The simplification of using only two radiative bands (visible and near infrared) ~~might cause some biases for the results in~~ may introduce biases in the results at certain wavelengths.

~~The use~~ Using of the L2SM and the LZ approaches requires the use of SIF spectra ~~in the~~ for unit conversion from the modelled ~~units~~ to observed units (see Section 2.6). ~~In this work we used for~~ For the LZ approach~~spectra that were~~ , we used spectra measured in a Finnish Scots pine forest. To extend this approach ~~further~~ to other PFTs, it would be necessary to use ~~other~~ different measured SIF spectra. This approach has limitations in terms of generalizability ~~, as~~ because these spectra differ between species ~~and therefore~~ (Liu et al., 2025; Magney et al., 2017). Therefore, using a single spectrum for a PFT may introduce uncertainties. Furthermore, the spectral shape of SIF emission changes under stress conditions~~, e.g. the~~ . For example, photosystems I and II ~~have different responses to stress (?)~~respond differently to stress (Magney et al., 2019a), which will further limit our approach, and require careful investigation of the stress effects. For the L2SM approach we used ~~an~~ a theoretical estimate of the in vivo spectrum. ~~This approach would also benefit from further~~ Further testing with observed ~~spectra~~in vivo spectra would also benefit this approach.

~~The~~

### 4.5 Uncertainties in the observations

Using the Fraunhofer line method ~~used~~ with PhotoSpec instruments is less susceptible to atmospheric attenuation than using the oxygen lines with FloX. ~~The~~ At FI-Sod, the distance from the soil for FloX ~~at FI-Sod~~ was around 19-20 m, and the distance to the canopy was less. Therefore, the measurement distance is less than 20 ~~m, which is considered the threshold for needing the data~~ meters, the threshold at which the data must to be corrected for atmospheric effects (Sabater et al., 2018; van der Tol et al., 2023). FI-Sod ~~also has a sparse canopy compared to~~ has a sparser canopy than the other sites, which ~~may imply~~ implies that the footprint of the observing optical ~~fibre~~ fiber is susceptible to environmental influences other than the canopy, such as

~~understory.~~ the understory. The nearly linear relationship between GPP and SIF in the observations may indicate understory contribution (Fig. **??**a).

The measurements that we used have several ~~uncertainties~~sources of uncertainty. The tower SIF observations are relatively new observations and have uncertainties related to instrumentation, the retrieval method, and ~~spatial match of~~ the spatial matching of the optical and flux footprints (Buman et al., 2022; Cendrero-Mateo et al., 2019; Pacheco-Labrador et al., 2019). Our results showed that using averaging for the model evaluation ~~might~~ could be a useful ~~way to use these data. Looking at the whole diurnal cycle showed some~~ method for evaluating the model. The eddy covariance observations are subject to uncertainty due to the measuring equipment, the heterogeneity of the footprint, and the stochastic nature of turbulence (Richardson et al., 2006). Gap-filling introduces additional uncertainties to the data (Vekuri et al., 2025).

Comparing the satellite observations to a site level observations introduces several uncertainties. The fact that the TROPOSIF estimates remain close to zero by the end of May, despite the GPP levels advancing towards summer levels, indicates that these observations must be handled with caution. Clouds make interpreting the signal more challenging, which is why we used the strict cloud filtering criterion recommended for this type of study. The is a large mismatch in scale between the satellite and flux tower observations. However, constraining the region did not improve the modelling results. This may be because more points help to smooth out the random error of the satellite observations. When only pixels where the site was located were chosen from the satellite retrievals, there were so few points that no significant seasonal cycle was detected at the sites (data not shown). The data aggregation performed for TROPOSIF involves averaging over several viewing geometries because the viewing angle varies due to the wide swath. This introduces additional uncertainty to the data. The land cover classes within the TROPOSIF product that are derived from the MODIS product obviously have issues in the high latitudes, which is a known issue (Liang et al., 2019). However, the land cover class does not impact the retrieved SIF because it is only used to identify water bodies and glaciers. An overall uncertainty of $\sim 0.50$ $\mathrm{Wm^{-2}s^{-1}nm^{-1}sr^{-1}}$ has been found for the TROPOSIF product, as reported in Du et al. (2023), which emphasizes that the low values during the shoulder seasons for these northern sites are very uncertain. Site heterogeneity influences the the accuracy of TROPOSIF (Du et al., 2023), as do the geolocation shifts (Zeng et al., 2024).

### 4.6 Model uncertainties and limitations

Our model only simulates one plant functional type per site and is horizontally homogeneous. Thus, the influence of the understory is ignored, even though it may be relevant, e.g., at FI-Sod, where the site has a low LAI and the footprint of the tower SIF observation is static. QUINCY has a representation of clumping, but L2SM does not. Therefore, including clumping in the radiative transfer of SIF in L2SM could improve the results in coniferous forests. Examining the entire diurnal cycle revealed discrepancies between the simulation results and the observations, ~~potentially revealing~~ which could be due to the effects of shadows~~that would require more~~. More rigorous modelling tools, such as ~~using~~ a 3D description ~~for the forest structure. The fact that the simulated SIF gave similar values for the same GPP value depending on the time of day~~ of forest structure, would be required to account for these effects. In reality, directional effects also influence the observed optical signal, but our approach did not account for them (Hilker et al., 2008b, a). A comparison of simulated and observation based estimates

of aPAR from FloX box and PAR sensors revealed that the model's inability to capture certain dynamics observed by the FloX box may be due to its small footprint.

The scatter of the observed SIF against the observed GPP values, as well as the fact that model was unable to fully capture this behaviour (Fig. 6)~~gives reason to look deeper, ~~, raises questions about whether the simulated SIF ~~gives~~ provides reasonable results in ~~water stressed~~ water-stressed conditions. However, due to the scattered nature of the SIF observations, ~~it was not straightforward to make a detailed analysis of that. The eddy covariance observations have uncertainties associated with measuring equipment, heterogeneity of the footprint and stochastic nature of turbulence (Richardson et al., 2006). The gap-filling introduces more uncertainties to the data (Vekuri et al., 2025)~~having a more comprehensive dataset than the one used in this study would be helpful.

### 4.7 Role of sustained NPQ

Our results showed a strong influence of sustained NPQ for these sites, where the plants cannot use the energy of the incoming radiation due to temperature constraints and winter dormancy (see also (Pierrat et al., 2024)). ChlF is closely related to photosynthesis, as both result from the functioning of the leaf biochemical machinery. In the current framework, there is currently no feedback from the modelling of SIF back to the photosynthesis part of the QUINCY model, so describing the $NPQ_s$ did not influence modelling of GPP. However, similar mechanism based on state of acclimation as used in $NPQ_s$ has been implemented for spring recovery of GPP in the QUINCY model already earlier.

In general, simulating NPQ has been a challenge in the modelling community, as it is composed of many processes (Zaks et al., 2013) and active measurements have been needed to quantify it. However, recent advances in the use of spectral imaging of xanthophyll cycle pigments are advancing and making it possible to quantify NPQ also from the optical observations (Pescador-Dionisio et al., 2025; Van Wittenberghe et al., 2024), thus making remote sensing of NPQ feasible. Also some studies have combined vegetation indices to help in parameterization of NPQ (Jiang et al., 2023). Some new parameterizations for NPQ based on site-level observations have also become available (Martini et al., 2022).

A more thorough analysis on additional data at Sodankylä (including longer time series of the FloX observations and active ChlF observations with MoniPAM) will be carried out to develop a formulation for sustained NPQ applicable to the site. The current results showed (when comparing the spring time against satellite observations, Fig. S16) that the formulation that was successful at other sites likely caused a too early increase in simulated SIF in spring. It could be that the colder temperature and light regime of high latitudes together causes the FI-Sod has a different dormancy level and mechanisms for coping with stress caused by winter conditions than the sites located in North America. Study from South Korean evergreen coniferous forest showed lower values for observed chlorophyll fluorescence yield ($\Phi_F$) showed lower values of $\Phi_F$ for low temperatures than our parameterization allowed (Fig. S12). Therefore, it is likely that the parameterization could be improved for the FI-Sod, while still maintaining realistic values for $\Phi_F$. While similar parameterization for GPP based on state of acclimation was successful across the sites, the same was not true for a parameterization based on similar principles for sustained NPQ. This could be caused by the closer link of the ChlF to pigment pool changes than GPP (Kim et al., 2021). The cold protection mechanisms of conifers are complex and include additionally changes in the absorption cross-section of the

antenna complexes, as well as down-regulation of photosystem II activity with simultaneous energy tranfer from photosystem II to photosystem I (Bag et al., 2020). The ratio between GPP and SIF has been shown to vary in low temperatures in earlier studies (Chen et al., 2022, 2025) and it is important to be able to model dynamics of this behaviour so that we understand the coupling between GPP and SIF.

A recent study combining PAM observations worldwide evaluated the photosynthetic capacity of photosystem II ~~and showed that it~~ (Neri et al., 2024). The study showed that this capacity depends more on the temperature regime of the ~~vegetation's environment~~ environment where the vegetation grows than on the ~~plant species (Neri et al., 2024)~~species of plant. The study also ~~provided a quantification~~ quantified of this dependence. The ~~final aim will be~~ ultimate goal is to obtain a sufficiently general parameterization for the ~~whole~~ entire coniferous evergreen forest region, using the results of (Neri et al., 2024), possibly with the help of TROPOMI observations. ~~The use of~~ Using the same model for ~~both~~ photosynthesis and ChlF (Johnson and Berry, 2021) could potentially circumvent this problem. However, the current photosynthesis ~~formulation of QUINCY has a direct influence of nitrogen on the photosynthesis parameters~~ parameters in QUINCY are directly influenced by nitrogen content and also leaf chlorophyll content is closely coupled to photosynthesis (Thum et al., 2025). Leaf chlorophyll content ~~can potentially~~ could be useful as a metric related to nitrogen cycling in model evaluation (Miinalainen et al., 2025)~~, which is much needed (Kou-Giesbrecht et al., 2023). In addition~~. This is a much-needed metric (Kou-Giesbrecht et al., 2023). Additionally, the amount of leaf chlorophyll influences how much of the SIF emitted from ~~the leaves~~ leaves that is attenuated in the canopy within the visible spectrum. Therefore, ~~a model that includes~~ including both leaf chlorophyll and SIF ~~included~~ in a model such as QUINCY would be beneficial for understanding Earth system processes and their temporal variations. The amount of chlorophyll in leaves also affects the shape of the SIF spectrum~~, and as~~ . Since we used a fixed SIF spectrum to convert from the total ~~flux of SIF~~ SIF flux to SIF at a given wavelength (Magney et al., 2019b), this ~~would also~~ topic could benefit from some further investigation.

## 5 Conclusions

We have implemented chlorophyll fluorescence into the QUINCY model and tested different canopy transfer approaches of the SIF signal. On a seasonal scale, many of the approaches performed similarly, and did not show clear differences in performance when looking at day-to-day variation and the ability to simulate different times of day. The magnitude of the tower-based SIF observations was greatly overestimated in the simulations, but the timing and seasonality were captured successfully. Of the approaches studied, L2SM showed consistent performance across the sites and is computationally feasible to implement in a large-scale model. ~~Still,~~ We hypothesize that the consistent overestimation ~~of SIF suggests the~~ might arise from the misrepresentation of conifer leaves and canopy with the commonly used 1D canopy, and leaf plate-theory-based radiative transfer models. However, no fluorescence emission has been implemented in needle-like leaf radiative transfer models, and 3D ~~structure of conifer forest should be better accounted for by modelsand~~ canopy transfer modules are too computationally demanding for TBMs. Thus, simpler modeling solutions should be explored to improve the representation of fluorescence emission in conifer forests, with the help of proximal sensing measurements ~~.~~

Sustained NPQ was relevant in decoupling the simulated SIF from the observed absorbed PAR and the same parameterization improved model performance at the North American sites but appeared less suitable at the Finnish site. ~~The~~ This process is likely linked to the air temperature regime of the sites. The ~~satellite TROPOSIF product~~ TROPOSIF product from satellite was able to capture the low spring values observed at CA-Obs and could therefore probably serve as additional data when implementing the parameterization of sustained NPQ in a global model. However, for more northern site FI-Sod the amount of points in spring was sparse and an increase in TROPOSIF occurred later than for GPP. Use of TROPOSIF observations additionally in model evaluation and development seems feasible, given that the springtime behaviour seems to follow better site level observations of SIF than absorbed PAR.

The next step of this work will be to extend it to other ecosystems, using both in situ and satellite observations as evaluation data. ~~SIF observations have also been shown to be closely linked to the latent heat flux observations and we will extend our analysis also to include these.~~ Together with QUINCY's diagnostic leaf chlorophyll content, a variable which can be observed from space, this work brings QUINCY closer to being a tool for comprehensive analysis of biogeochemical cycles. ~~In addition, the knowledge gained from this work will pave the way for data assimilation studies using SIF observations measured at different scales.~~

*Code and data availability.* The scientific part of the QUINCY code is available under a GPL v3 license. The source code is available online (https://doi.org/10.17871/quincy-model-2019), but its access is restricted to registered users. Readers interested in running the model should request a username and password via the Git repository.

L2SM-code by T. Quaife is available at Zenodo in doi: 10.5281/zenodo.13753268. The FloX observations with meteorology and $CO_2$ fluxes from Sodankylä are available at https://zenodo.org/records/12725765. The PhotoSpec observations and $CO_2$ flux observations from CA-Obs are available at https://zenodo.org/records/10048770 and from US-NR1 at https://data.caltech.edu/records/meh5c-wy279. The meteorological data for the North American sites is available from Ameriflux (https://ameriflux.lbl.gov/). The simulation results of SIF are available at https://fmi.b2share.csc.fi/records/8847a0c06c374668b01e345094d373cd.

*Author contributions.* TT designed the study, implemented Fluspect to version of QUINCY including mSCOPE, performed all the simulations and analysis and was responsible for the first draft of the manuscript. ZP and JS conducted the Photospec observations at CA-Obs, where AB and BJ were responsible for the $CO_2$ flux and meteorological observations. TM and JS were responsible for the PhotoSpec observations at US-NR1. MH conducted the FloX observations at FI-Sod in collaboration with HL. HL contributed the satellite data. MA was responsible for the $CO_2$ flux and meteorological observations at FI-Sod. JPL made original implementation of mSCOPE to the QUINCY model. TQ provided the L2SM code and help with its use as well as the code for the unit conversion. SZ provided help with the QUINCY model. All the authors contributed to discussing the results and writing of the manuscript.

*Competing interests.* At least one of the (co)-authors is a member of the editorial board of Biogeosciences..

*Disclaimer.* TEXT

*Acknowledgements.* TT acknowledges funding from Research Council of Finland (RESEMON project, grant number 330165; and 337552). TQ received funding under UKRI NERC grant NE/W006596/1 Structure, Photosynthesis and Light In Canopy Environments (SPLICE) which supported development of the L2SM model. HL and MH acknowledge funding from the Research Council of Finland (grant numbers 337552, 359196, and 353082). We acknowledge the AmeriFlux sites for their data records. In addition, funding for AmeriFlux data resources was provided by the U.S. Department of Energy's Office of Science. We acknowledge the Ministry of Transport and Communications through the Integrated Carbon Observing System (ICOS) research and ICOS Finland. The FloX observations were done as part of European Space Agency funded project through contract number 4000131497 within the Carbon science Cluster. We thank Tommaso Julitta for help with data processing of the FloX data. Scientific programmers Dr. Jan Engel and Dr. Julia Nabel are thanked for technical support and maintenance of the QUINCY code. TM, ZP and JS acknowledge funding by NASA's Earth Science Division IDS (awards 80NSSC17K0108 at UCLA, 80NSSC17K0110 at JPL) and ABoVE programs (award 80NSSC19M0130). ZP work was supported by a National Science Foundation Graduate Research Fellowship under Grant No. DGE-1650604 and DGE-2034835. We thank the reviewers whose constructive comments helped to improve the manuscript.

## References


Adams, W. W., Muller, O., Cohu, C. M., and Demmig-Adams, B.: Photosystem II Efficiency and Non-Photochemical Fluorescence Quenching in the Context of Source-Sink Balance, pp. 503–529, Springer Netherlands, Dordrecht, https://doi.org/10.1007/978-94-017-9032-1_23, 2014.

Alonso, L., Gomez-Chova, L., Vila-Frances, J., Amoros-Lopez, J., Guanter, L., Calpe, J., and Moreno, J.: Improved Fraunhofer Line Discrimination Method for Vegetation Fluorescence Quantification, IEEE Geoscience and Remote Sensing Letters, 5, 620–624, https://doi.org/10.1109/LGRS.2008.2001180, 2008.

Aurela, M., Lohila, A., Tuovinen, J.-P., Hatakka, J., Penttilä, T., and Laurila, T.: Carbon dioxide and energy flux measurements in four northern-boreal ecosystems at Pallas, Boreal Environment Research, 20, 455–473, 2015.

Bacour, C., Maignan, F., MacBean, N., Porcar-Castell, A., Flexas, J., Frankenberg, C., Peylin, P., Chevallier, F., Vuichard, N., and Bastrikov, V.: Improving Estimates of Gross Primary Productivity by Assimilating Solar-Induced Fluorescence Satellite Retrievals in a Terrestrial Biosphere Model Using a Process-Based SIF Model, Journal of Geophysical Research: Biogeosciences, 124, 3281–3306, https://doi.org/https://doi.org/10.1029/2019JG005040, 2019.

Bag, P., Chukhutsina, V., Zhang, Z., Paul, S., Ivanov, A. G., Shutova, T., Croce, R., Holzwarth, A. R., and Jansson, S.: Direct energy transfer from Photosystem II to Photosystem I confers winter sustainability in Scots pine, Nature Communications, 11, 6388, https://doi.org/10.1038/s41467-020-20137-9, 2020.

Baker, N. R.: Chlorophyll Fluorescence: A Probe of Photosynthesis In Vivo, Annual Review of Plant Biology, 59, 89–113, https://doi.org/10.1146/annurev.arplant.59.032607.092759, 2008.

Balde, H., Hmimina, G., Goulas, Y., Latouche, G., and Soudani, K.: Synergy between TROPOMI sun-induced chlorophyll fluorescence and MODIS spectral reflectance for understanding the dynamics of gross primary productivity at Integrated Carbon Observatory System (ICOS) ecosystem flux sites, Biogeosciences, 20, 1473–1490, https://doi.org/10.5194/bg-20-1473-2023, 2023.

Barr, A. G., Black, T., Hogg, E., Kljun, N., Morgenstern, K., and Nesic, Z.: Inter-annual variability in the leaf area index of a boreal aspen-hazelnut forest in relation to net ecosystem production, Agricultural and Forest Meteorology, 126, 237–255, https://doi.org/10.1016/j.agrformet.2004.06.011, 2004.

Bonan, G. B.: Forests and Climate Change: Forcings, Feedbacks, and the Climate Benefits of Forests, Science, 320, 1444–1449, https://doi.org/10.1126/science.1155121, 2008.

Bowling, D. R., Logan, B. A., Hufkens, K., Aubrecht, D. M., Richardson, A. D., Burns, S. P., Anderegg, W. R., Blanken, P. D., and Eiriksson, D. P.: Limitations to winter and spring photosynthesis of a Rocky Mountain subalpine forest, Agricultural and Forest Meteorology, 252, 241–255, https://doi.org/10.1016/j.agrformet.2018.01.025, 2018.

Bradshaw, C. J. and Warkentin, I. G.: Global estimates of boreal forest carbon stocks and flux, Global and Planetary Change, 128, 24–30, https://doi.org/10.1016/j.gloplacha.2015.02.004, 2015.

Buman, B., Hueni, A., Colombo, R., Cogliati, S., Celesti, M., Julitta, T., Burkart, A., Siegmann, B., Rascher, U., Drusch, M., and Damm, A.: Towards consistent assessments of in situ radiometric measurements for the validation of fluorescence satellite missions, Remote Sensing of Environment, 274, 112 984, https://doi.org/https://doi.org/10.1016/j.rse.2022.112984, 2022.

Burns, S. P., Blanken, P. D., Turnipseed, A. A., Hu, J., and Monson, R. K.: The influence of warm-season precipitation on the diel cycle of the surface energy balance and carbon dioxide at a Colorado subalpine forest site, Biogeosciences, 12, 7349–7377, https://doi.org/10.5194/bg-12-7349-2015, 2015.

Campbell, G. S. and Norman, J. M.: An Introduction to Environmental Biophysics, Springer, 1998.

Cendrero-Mateo, M. P., Wieneke, S., Damm, A., Alonso, L., Pinto, F., Moreno, J., Guanter, L., Celesti, M., Rossini, M., Sabater, N., Cogliati, S., Julitta, T., Rascher, U., Goulas, Y., Aasen, H., Pacheco-Labrador, J., and Mac Arthur, A.: Sun-Induced Chlorophyll Fluorescence III: Benchmarking Retrieval Methods and Sensor Characteristics for Proximal Sensing, Remote Sensing, 11, 962, https://doi.org/10.3390/rs11080962, 2019.

Chen, J., Liu, X., Ma, Y., and Liu, L.: Effects of Low Temperature on the Relationship between Solar-Induced Chlorophyll Fluorescence and Gross Primary Productivity across Different Plant Function Types, Remote Sensing, 14, https://doi.org/10.3390/rs14153716, 2022.

Chen, R., Liu, L., Liu, X., Wong, C. Y. S., and Ensminger, I.: Temperature-Dependent Relationship Between Solar-Induced Chlorophyll Fluorescence and Photosynthesis in Evergreen Needleleaf Forests, IEEE Transactions on Geoscience and Remote Sensing, 63, 1–11, https://doi.org/10.1109/TGRS.2025.3620306, 2025.

Damm, A., Guanter, L., Paul-Limoges, E., van der Tol, C., Hueni, A., Buchmann, N., Eugster, W., Ammann, C., and Schaepman, M.: Far-red sun-induced chlorophyll fluorescence shows ecosystem-specific relationships to gross primary production: An assessment based on observational and modeling approaches, Remote Sensing of Environment, 166, 91–105, https://doi.org/https://doi.org/10.1016/j.rse.2015.06.004, 2015.

Dechant, B., Ryu, Y., Badgley, G., Köhler, P., Rascher, U., Migliavacca, M., Zhang, Y., Tagliabue, G., Guan, K., Rossini, M., Goulas, Y., Zeng, Y., Frankenberg, C., and Berry, J. A.: NIRVP: A robust structural proxy for sun-induced chlorophyll fluorescence and photosynthesis across scales, Remote Sensing of Environment, 268, 112 763, https://doi.org/https://doi.org/10.1016/j.rse.2021.112763, 2022.

Demmig-Adams, B., Koh, S.-C., Cohu, C. M., Muller, O., Stewart, J. J., and Adams, W. W.: Non-Photochemical Fluorescence Quenching in Contrasting Plant Species and Environments, pp. 531–552, Springer Netherlands, Dordrecht, https://doi.org/10.1007/978-94-017-9032-1_24, 2014.

Du, S., Liu, X., Chen, J., Duan, W., and Liu, L.: Addressing validation challenges for TROPOMI solar-induced chlorophyll fluorescence products using tower-based measurements and an NIRv-scaled approach, Remote Sensing of Environment, 290, 113 547, https://doi.org/https://doi.org/10.1016/j.rse.2023.113547, 2023.

Fan, L., Kato, T., Miyauchi, T., Buareal, K., Morozumi, T., and Ono, K.: Data Assimilation of Solar-Induced Chlorophyll Fluorescence Improves Gross Primary Production Simulation by a Process-Based VISIT-SIF Model in a Rice Paddy, Journal of Geophysical Research: Biogeosciences, 130, e2024JG008 280, https://doi.org/https://doi.org/10.1029/2024JG008280, e2024JG008280 2024JG008280, 2025.

Farquhar, G. D., Von Caemmerer, S., and Berry, J. A.: A biochemical model of photosynthetic CO2 assimilation in leaves of C3 species, Planta, 149, 78–90, https://doi.org/10.1007/BF00386231, 1980.

Frankenberg, C., Fisher, J. B., Worden, J., Badgley, G., Saatchi, S. S., Lee, J.-E., Toon, G. C., Butz, A., Jung, M., Kuze, A., and Yokota, T.: New global observations of the terrestrial carbon cycle from GOSAT: Patterns of plant fluorescence with gross primary productivity: Chlorophyll fluorescence from space, Geophysical Research Letters, 38, n/a–n/a, https://doi.org/10.1029/2011GL048738, 2011.

Frankenberg, C., O'Dell, C., Berry, J., Guanter, L., Joiner, J., Köhler, P., Pollock, R., and Taylor, T. E.: Prospects for chlorophyll fluorescence remote sensing from the Orbiting Carbon Observatory-2, Remote Sensing of Environment, 147, 1–12, https://doi.org/https://doi.org/10.1016/j.rse.2014.02.007, 2014.

Friedl, M. and Sulla-Menashe, D.: MODIS/Terra+Aqua Land Cover Type Yearly L3 Global 0.05Deg CMG V061, https://doi.org/10.5067/MODIS/MCD12C1.061, data set, 2022.

Genty, B., Briantais, J.-M., and Baker, N. R.: The relationship between the quantum yield of photosynthetic electron transport and quenching of chlorophyll fluorescence, Biochimica et Biophysica Acta (BBA) - General Subjects, 990, 87–92, https://doi.org/https://doi.org/10.1016/S0304-4165(89)80016-9, 1989.

Gopalakrishnan, R., Korhonen, L., Mõttus, M., Rautiainen, M., Hovi, A., Mehtätalo, L., Maltamo, M., Peltola, H., and Packalen, P.: Evaluation of a forest radiative transfer model using an extensive boreal forest inventory database, Science of Remote Sensing, 8, 100 098, https://doi.org/10.1016/j.srs.2023.100098, 2023.

Gordon, H. R.: Diffuse reflectance of the ocean: The theory of its augmentation by chlorophyll a fluorescence at 685 nm, Applied Optics, 18, 1161–1166, https://doi.org/10.1364/AO.18.001161, 1979.

Grossmann, K., Frankenberg, C., Magney, T. S., Hurlock, S. C., Seibt, U., and Stutz, J.: PhotoSpec: A new instrument to measure spatially distributed red and far-red Solar-Induced Chlorophyll Fluorescence, Remote Sensing of Environment, 216, 311–327, https://doi.org/10.1016/j.rse.2018.07.002, 2018.

Gu, L., Han, J., Wood, J. D., Chang, C. Y., and Sun, Y.: Sun-induced Chl fluorescence and its importance for biophysical modeling of photosynthesis based on light reactions, New Phytologist, 223, 1179–1191, https://doi.org/10.1111/nph.15796, 2019.

Guanter, L., Frankenberg, C., Dudhia, A., Lewis, P. E., Gómez-Dans, J., Kuze, A., Suto, H., and Grainger, R. G.: Retrieval and global assessment of terrestrial chlorophyll fluorescence from GOSAT space measurements, Remote Sensing of Environment, 121, 236–251, https://doi.org/https://doi.org/10.1016/j.rse.2012.02.006, 2012.

Guanter, L., Aben, I., Tol, P., Krijger, J. M., Hollstein, A., Köhler, P., Damm, A., Joiner, J., Frankenberg, C., and Landgraf, J.: Potential of the TROPOspheric Monitoring Instrument (TROPOMI) onboard the Sentinel-5 Precursor for the monitoring of terrestrial chlorophyll fluorescence, Atmospheric Measurement Techniques, 8, 1337–1352, https://doi.org/10.5194/amt-8-1337-2015, 2015.

Guanter, L., Bacour, C., Schneider, A., Aben, I., van Kempen, T. A., Maignan, F., Retscher, C., Köhler, P., Frankenberg, C., Joiner, J., and Zhang, Y.: The TROPOSIF global sun-induced fluorescence dataset from the Sentinel-5P TROPOMI mission, Earth System Science Data, 13, 5423–5440, https://doi.org/10.5194/essd-13-5423-2021, 2021.

Hao, D., Zeng, Y., Qiu, H., Biriukova, K., Celesti, M., Migliavacca, M., Rossini, M., Asrar, G. R., and Chen, M.: Practical approaches for normalizing directional solar-induced fluorescence to a standard viewing geometry, Remote Sensing of Environment, 255, 112 171, https://doi.org/10.1016/j.rse.2020.112171, 2021.

Hastie, T., Tibshirani, R., and Friedman, J.: The Elements of Statistical Learning, Springer, 2009.

Hilker, T., Coops, N. C., Hall, F. G., Black, T. A., Wulder, M. A., Nesic, Z., and Krishnan, P.: Separating physiologically and directionally induced changes in PRI using BRDF models, Remote Sensing of Environment, 112, 2777–2788, https://doi.org/https://doi.org/10.1016/j.rse.2008.01.011, 2008a.

Hilker, T., Coops, N. C., Schwalm, C. R., Jassal, R. S., Black, T. A., and Krishnan, P.: Effects of mutual shading of tree crowns on prediction of photosynthetic light-use efficiency in a coastal Douglas-fir forest, Tree Physiology, 28, 825–834, https://doi.org/10.1093/treephys/28.6.825, 2008b.

Jacquemoud, S. and Baret, F.: PROSPECT: A model of leaf optical properties spectra, Remote Sensing of Environment, 34, 75–91, https://doi.org/https://doi.org/10.1016/0034-4257(90)90100-Z, 1990.

Jiang, H., Liu, Z., Wang, J., Yang, P., Zhang, R., Zhang, X., and Zheng, P.: Combining Chlorophyll Fluorescence and Vegetation Reflectance Indices to Estimate Non-Photochemical Quenching (NPQ) of Rice at the Leaf Scale, Remote Sensing, 15, https://doi.org/10.3390/rs15174222, 2023.

Johnson, J. E. and Berry, J. A.: The role of Cytochrome b6f in the control of steady-state photosynthesis: a conceptual and quantitative model, Photosynthesis Research, 148, 101–136, https://doi.org/10.1007/s11120-021-00840-4, 2021.

Joiner, J., Yoshida, Y., Vasilkov, A. P., Yoshida, Y., Corp, L. A., and Middleton, E. M.: First observations of global and seasonal terrestrial chlorophyll fluorescence from space, Biogeosciences, 8, 637–651, https://doi.org/10.5194/bg-8-637-2011, 2011.

Joiner, J., Guanter, L., Lindstrot, R., Voigt, M., Vasilkov, A. P., Middleton, E. M., Huemmrich, K. F., Yoshida, Y., and Frankenberg, C.: Global monitoring of terrestrial chlorophyll fluorescence from moderate-spectral-resolution near-infrared satellite measurements: methodology, simulations, and application to GOME-2, Atmospheric Measurement Techniques, 6, 2803–2823, https://doi.org/10.5194/amt-6-2803-2013, 2013.

Joiner, J., Yoshida, Y., Köehler, P., Campbell, P., Frankenberg, C., van der Tol, C., Yang, P., Parazoo, N., Guanter, L., and Sun, Y.: Systematic Orbital Geometry-Dependent Variations in Satellite Solar-Induced Fluorescence (SIF) Retrievals, Remote Sensing, 12, https://doi.org/10.3390/rs12152346, 2020.

Kim, J., Ryu, Y., Dechant, B., Lee, H., Kim, H. S., Kornfeld, A., and Berry, J. A.: Solar-induced chlorophyll fluorescence is non-linearly related to canopy photosynthesis in a temperate evergreen needleleaf forest during the fall transition, Remote Sensing of Environment, 258, 112 362, https://doi.org/https://doi.org/10.1016/j.rse.2021.112362, 2021.

Knorr, W., Williams, M., Thum, T., Kaminski, T., Voßbeck, M., Scholze, M., Quaife, T., Smallman, T. L., Steele-Dunne, S. C., Vreugdenhil, M., Green, T., Zaehle, S., Aurela, M., Bouvet, A., Bueechi, E., Dorigo, W., El-Madany, T. S., Migliavacca, M., Honkanen, M., Kerr, Y. H., Kontu, A., Lemmetyinen, J., Lindqvist, H., Mialon, A., Miinalainen, T., Pique, G., Ojasalo, A., Quegan, S., Rayner, P. J., Reyes-Muñoz, P., Rodríguez-Fernández, N., Schwank, M., Verrelst, J., Zhu, S., Schüttemeyer, D., and Drusch, M.: A comprehensive land-surface vegetation model for multi-stream data assimilation, D&B v1.0, Geoscientific Model Development, 18, 2137–2159, https://doi.org/10.5194/gmd-18-2137-2025, 2025.

Koffi, E. N., Rayner, P. J., Norton, A. J., Frankenberg, C., and Scholze, M.: Investigating the usefulness of satellite-derived fluorescence data in inferring gross primary productivity within the carbon cycle data assimilation system, Biogeosciences, 12, 4067–4084, https://doi.org/10.5194/bg-12-4067-2015, 2015.

Kou-Giesbrecht, S., Arora, V. K., Seiler, C., Arneth, A., Falk, S., Jain, A. K., Joos, F., Kennedy, D., Knauer, J., Sitch, S., O'Sullivan, M., Pan, N., Sun, Q., Tian, H., Vuichard, N., and Zaehle, S.: Evaluating nitrogen cycling in terrestrial biosphere models: a disconnect between the carbon and nitrogen cycles, Earth System Dynamics, 14, 767–795, https://doi.org/10.5194/esd-14-767-2023, 2023.

Kull, O. and Kruijt, B.: Leaf photosynthetic light response: a mechanistic model for scaling photosynthesis to leaves and canopies, Functional Ecology, 12, 767–777, 1998.

Kuze, A., Suto, H., Nakajima, M., and Hamazaki, T.: Thermal and near infrared sensor for carbon observation Fourier-transform spectrometer on the Greenhouse Gases Observing Satellite for greenhouse gases monitoring, Appl. Opt., 48, 6716–6733, https://doi.org/10.1364/AO.48.006716, 2009.

Köhler, P., Frankenberg, C., Magney, T. S., Guanter, L., Joiner, J., and Landgraf, J.: Global Retrievals of Solar-Induced Chlorophyll Fluorescence With TROPOMI: First Results and Intersensor Comparison to OCO-2, Geophysical Research Letters, 45, 10,456–10,463, https://doi.org/https://doi.org/10.1029/2018GL079031, 2018.

Lee, J., Berry, J. A., Van Der Tol, C., Yang, X., Guanter, L., Damm, A., Baker, I., and Frankenberg, C.: Simulations of chlorophyll fluorescence incorporated into the Community Land Model version 4, Global Change Biology, 21, 3469–3477, https://doi.org/10.1111/gcb.12948, 2015.

Li, R., Lombardozzi, D., Shi, M., Frankenberg, C., Parazoo, N. C., Köhler, P., Yi, K., Guan, K., and Yang, X.: Representation of Leaf-to-Canopy Radiative Transfer Processes Improves Simulation of Far-Red Solar-Induced Chlorophyll Fluorescence in the Community Land Model Version 5, Journal of Advances in Modeling Earth Systems, 14, e2021MS002 747, https://doi.org/https://doi.org/10.1029/2021MS002747, e2021MS002747 2021MS002747, 2022.

Liang, L., Liu, Q., Liu, G., Li, H., and Huang, C.: Accuracy Evaluation and Consistency Analysis of Four Global Land Cover Products in the Arctic Region, Remote Sensing, 11, https://doi.org/10.3390/rs11121396, 2019.

Liu, W., Mõttus, M., Malenovský, Z., Shi, S., Alonso, L., Atherton, J., and Porcar-Castell, A.: An in situ approach for validation of canopy chlorophyll fluorescence radiative transfer models using the full emission spectrum, Remote Sensing of Environment, 316, 114 490, https://doi.org/https://doi.org/10.1016/j.rse.2024.114490, 2025.

Liu, X., Liu, L., Hu, J., Guo, J., and Du, S.: Improving the potential of red SIF for estimating GPP by downscaling from the canopy level to the photosystem level, Agricultural and Forest Meteorology, 281, 107 846, https://doi.org/10.1016/j.agrformet.2019.107846, 2020.

MacBean, N., Maignan, F., Bacour, C., Lewis, P., Peylin, P., Guanter, L., Köhler, P., Gómez-Dans, J., and Disney, M.: Strong constraint on modelled global carbon uptake using solar-induced chlorophyll fluorescence data, Scientific Reports, 8, 1973, https://doi.org/10.1038/s41598-018-20024-w, 2018.

Magney, T. and Frankenberg, C.: Chlorophyll fluorescence spectra for a wide range of species and conditions, https://doi.org/10.22002/D1.1226, funding by NASA, 2019.

Magney, T. S., Frankenberg, C., Fisher, J. B., Sun, Y., North, G. B., Davis, T. S., Kornfeld, A., and Siebke, K.: Connecting active to passive fluorescence with photosynthesis: a method for evaluating remote sensing measurements of Chl fluorescence, New Phytologist, 215, 1594–1608, https://doi.org/https://doi.org/10.1111/nph.14662, 2017.

Magney, T. S., Bowling, D. R., Logan, B. A., Grossmann, K., Stutz, J., Blanken, P. D., Burns, S. P., Cheng, R., Garcia, M. A., Köhler, P., Lopez, S., Parazoo, N. C., Raczka, B., Schimel, D., and Frankenberg, C.: Mechanistic evidence for tracking the seasonality of photosynthesis with solar-induced fluorescence, Proceedings of the National Academy of Sciences, 116, 11 640–11 645, https://doi.org/10.1073/pnas.1900278116, 2019a.

Magney, T. S., Frankenberg, C., Köhler, P., North, G., Davis, T. S., Dold, C., Dutta, D., Fisher, J. B., Grossmann, K., Harrington, A., Hatfield, J., Stutz, J., Sun, Y., and Porcar-Castell, A.: Disentangling Changes in the Spectral Shape of Chlorophyll Fluorescence: Implications for Remote Sensing of Photosynthesis, Journal of Geophysical Research: Biogeosciences, 124, 1491–1507, https://doi.org/https://doi.org/10.1029/2019JG005029, 2019b.

Magney, T. S., Barnes, M. L., and Yang, X.: On the Covariation of Chlorophyll Fluorescence and Photosynthesis Across Scales, Geophysical Research Letters, 47, e2020GL091 098, https://doi.org/https://doi.org/10.1029/2020GL091098, e2020GL091098 2020GL091098, 2020.

Majasalmi, T. and Bright, R. M.: Evaluation of leaf-level optical properties employed in land surface models, Geoscientific Model Development, 12, 3923–3938, https://doi.org/10.5194/gmd-12-3923-2019, 2019.

Mäkelä, J., Knauer, J., Aurela, M., Black, A., Heimann, M., Kobayashi, H., Lohila, A., Mammarella, I., Margolis, H., Markkanen, T., Susiluoto, J., Thum, T., Viskari, T., Zaehle, S., and Aalto, T.: Parameter calibration and stomatal conductance formulation comparison for boreal forests with adaptive population importance sampler in the land surface model JSBACH, Geoscientific Model Development, 12, 4075–4098, https://doi.org/10.5194/gmd-12-4075-2019, 2019.

Malenovský, Z., Regaieg, O., Yin, T., Lauret, N., Guilleux, J., Chavanon, E., Duran, N., Janoutová, R., Delavois, A., Meynier, J., Medjdoub, G., Yang, P., van der Tol, C., Morton, D., Cook, B. D., and Gastellu-Etchegorry, J.-P.: Discrete anisotropic radiative transfer modelling of

solar-induced chlorophyll fluorescence: Structural impacts in geometrically explicit vegetation canopies, Remote Sensing of Environment, 263, 112 564, https://doi.org/https://doi.org/10.1016/j.rse.2021.112564, 2021.

Martini, D., Pacheco-Labrador, J., Perez-Priego, O., van der Tol, C., El-Madany, T. S., Julitta, T., Rossini, M., Reichstein, M., Christiansen, R., Rascher, U., Moreno, G., Martín, M. P., Yang, P., Carrara, A., Guan, J., González-Cascón, R., and Migliavacca, M.: Nitrogen and Phosphorus Effect on Sun-Induced Fluorescence and Gross Primary Productivity in Mediterranean Grassland, Remote Sensing, 11, https://doi.org/10.3390/rs11212562, 2019.

Martini, D., Sakowska, K., Wohlfahrt, G., Pacheco-Labrador, J., van der Tol, C., Porcar-Castell, A., Magney, T. S., Carrara, A., Colombo, R., El-Madany, T. S., Gonzalez-Cascon, R., Martín, M. P., Julitta, T., Moreno, G., Rascher, U., Reichstein, M., Rossini, M., and Migliavacca, M.: Heatwave breaks down the linearity between sun-induced fluorescence and gross primary production, New Phytologist, 233, 2415–2428, https://doi.org/https://doi.org/10.1111/nph.17920, 2022.

Maxwell, K. and Johnson, G. N.: Chlorophyll fluorescence—a practical guide, Journal of Experimental Botany, 51, 659–668, https://doi.org/10.1093/jexbot/51.345.659, 2000.

Meador, W. and Weaver, W.: Two-stream approximations to radiative transfer in planetary atmospheres: A unified description of existing methods and a new improvement, Journal of Atmospheric Sciences, 37, 630–643, 1980.

Medlyn, B. E., Duursma, R. A., Eamus, D., Ellsworth, D. S., Prentice, I. C., Barton, C. V. M., Crous, K. Y., De Angelis, P., Freeman, M., and Wingate, L.: Reconciling the optimal and empirical approaches to modelling stomatal conductance, Global Change Biology, 17, 2134–2144, https://doi.org/https://doi.org/10.1111/j.1365-2486.2010.02375.x, 2011.

Miinalainen, T., Ojasalo, A., Croft, H., Aurela, M., Peltoniemi, M., Caldararu, S., Zaehle, S., and Thum, T.: Evaluating the carbon and nitrogen cycles of the QUINCY terrestrial biosphere model using remotely-sensed data, EGUsphere, 2025, 1–40, https://doi.org/10.5194/egusphere-2025-2987, 2025.

Miller, J., Berger, M., Goulas, Y., Jacquemoud, S., Louis, J., Mohammed, G., Moise, N., Moreno, J., Moya, I., Pedròs, R., Verhoef, W., , and Zarco-Tejada, P.: Development of a Vegetation Fluorescence Canopy Model, ESTEC Contract No. 16365/02/NL/FF, Final Report, 2005.

Miyauchi, T., Saito, M., Noda, H. M., Ito, A., Kato, T., and Matsunaga, T.: Process-based modeling of solar-induced chlorophyll fluorescence with VISIT-SIF version 1.0, Geoscientific Model Development, 18, 2329–2347, https://doi.org/10.5194/gmd-18-2329-2025, 2025.

Mohammed, G. H., Colombo, R., Middleton, E. M., Rascher, U., Van Der Tol, C., Nedbal, L., Goulas, Y., Pérez-Priego, O., Damm, A., Meroni, M., Joiner, J., Cogliati, S., Verhoef, W., Malenovský, Z., Gastellu-Etchegorry, J.-P., Miller, J. R., Guanter, L., Moreno, J., Moya, I., Berry, J. A., Frankenberg, C., and Zarco-Tejada, P. J.: Remote sensing of solar-induced chlorophyll fluorescence (SIF) in vegetation: 50 years of progress, Remote Sensing of Environment, 231, 111 177, https://doi.org/10.1016/j.rse.2019.04.030, 2019.

Mäkelä, A., Hari, P., Berninger, F., Hänninen, H., and Nikinmaa, E.: Acclimation of photosynthetic capacity in Scots pine to the annual cycle of temperature, Tree Physiology, 24, 369–376, https://doi.org/10.1093/treephys/24.4.369, 2004.

Neri, P., Gu, L., and Song, Y.: The effect of temperature on photosystem II efficiency across plant functional types and climate, Biogeosciences, 21, 2731–2758, https://doi.org/10.5194/bg-21-2731-2024, 2024.

Niinemets, Ü., Kull, O., and Tenhunen, J. D.: An analysis of light effects on foliar morphology, physiology, and light interception in temperate deciduous woody species of contrasting shade tolerance, Tree Physiology, 18, 681–696, https://doi.org/10.1093/treephys/18.10.681, 1998.

NOA: FLUXNET Data Download, http://www.fluxdata.org/DataDownload/default.aspx, last access: 17 February 2015, 2007.

Norton, A. J., Rayner, P. J., Koffi, E. N., Scholze, M., Silver, J. D., and Wang, Y.-P.: Estimating global gross primary productivity using chlorophyll fluorescence and a data assimilation system with the BETHY-SCOPE model, Biogeosciences, 16, 3069–3093, https://doi.org/10.5194/bg-16-3069-2019, 2019.

Otto, J., Berveiller, D., Bréon, F.-M., Delpierre, N., Geppert, G., Granier, A., Jans, W., Knohl, A., Kuusk, A., Longdoz, B., Moors, E., Mund, M., Pinty, B., Schelhaas, M.-J., and Luyssaert, S.: Forest summer albedo is sensitive to species and thinning: how should we account for this in Earth system models?, Biogeosciences, 11, 2411–2427, https://doi.org/10.5194/bg-11-2411-2014, 2014.

Pacheco-Labrador, J., Hueni, A., Mihai, L., Sakowska, K., Julitta, T., Kuusk, J., Sporea, D., Alonso, L., Burkart, A., Cendrero-Mateo, M. P., Aasen, H., Goulas, Y., and Mac Arthur, A.: Sun-Induced Chlorophyll Fluorescence I: Instrumental Considerations for Proximal Spectroradiometers, Remote Sensing, 11, https://doi.org/10.3390/rs11080960, 2019.

Pan, Y., Birdsey, R. A., Phillips, O. L., Houghton, R. A., Fang, J., Kauppi, P. E., Keith, H., Kurz, W. A., Ito, A., Lewis, S. L., Nabuurs, G.-J., Shvidenko, A., Hashimoto, S., Lerink, B., Schepaschenko, D., Castanho, A., and Murdiyarso, D.: The enduring world forest carbon sink, Nature, 631, 563–569, https://doi.org/10.1038/s41586-024-07602-x, 2024.

Parazoo, N. C., Magney, T., Norton, A., Raczka, B., Bacour, C., Maignan, F., Baker, I., Zhang, Y., Qiu, B., Shi, M., MacBean, N., Bowling, D. R., Burns, S. P., Blanken, P. D., Stutz, J., Grossmann, K., and Frankenberg, C.: Wide discrepancies in the magnitude and direction of modeled solar-induced chlorophyll fluorescence in response to light conditions, Biogeosciences, 17, 3733–3755, https://doi.org/10.5194/bg-17-3733-2020, 2020.

Paul-Limoges, E., Damm, A., Hueni, A., Liebisch, F., Eugster, W., Schaepman, M. E., and Buchmann, N.: Effect of environmental conditions on sun-induced fluorescence in a mixed forest and a cropland, Remote Sensing of Environment, 219, 310–323, https://doi.org/10.1016/j.rse.2018.10.018, 2018.

Pescador-Dionisio, S., Cendrero-Mateo, M. P., Moncholí-Estornell, A., Robles-Fort, A., Arzac, M. I., Renau-Morata, B., Fernández-Marín, B., García-Plazaola, J. I., Molina, R. V., Rausell, C., Moreno, J., Nebauer, S. G., García-Robles, I., and Van Wittenberghe, S.: *In vivo* detection of spectral reflectance changes associated with regulated heat dissipation mechanisms complements fluorescence quantum efficiency in early stress diagnosis, New Phytologist, 245, 559–576, https://doi.org/10.1111/nph.20253, 2025.

Pierrat, Z., Nehemy, M. F., Roy, A., Magney, T., Parazoo, N. C., Laroque, C., Pappas, C., Sonnentag, O., Grossmann, K., Bowling, D. R., Seibt, U., Ramirez, A., Johnson, B., Helgason, W., Barr, A., and Stutz, J.: Tower-Based Remote Sensing Reveals Mechanisms Behind a Two-phased Spring Transition in a Mixed-Species Boreal Forest, Journal of Geophysical Research: Biogeosciences, 126, e2020JG006 191, https://doi.org/10.1029/2020JG006191, 2021.

Pierrat, Z., Magney, T., Parazoo, N. C., Grossmann, K., Bowling, D. R., Seibt, U., Johnson, B., Helgason, W., Barr, A., Bortnik, J., Norton, A., Maguire, A., Frankenberg, C., and Stutz, J.: Diurnal and Seasonal Dynamics of Solar-Induced Chlorophyll Fluorescence, Vegetation Indices, and Gross Primary Productivity in the Boreal Forest, Journal of Geophysical Research: Biogeosciences, 127, e2021JG006 588, https://doi.org/10.1029/2021JG006588, 2022a.

Pierrat, Z. A., Bortnik, J., Johnson, B., Barr, A., Magney, T., Bowling, D. R., Parazoo, N., Frankenberg, C., Seibt, U., and Stutz, J.: Forests for forests: combining vegetation indices with solar-induced chlorophyll fluorescence in random forest models improves gross primary productivity prediction in the boreal forest, Environmental Research Letters, 17, 125 006, https://doi.org/10.1088/1748-9326/aca5a0, 2022b.

Pierrat, Z. A., Magney, T., Maguire, A., Brissette, L., Doughty, R., Bowling, D. R., Logan, B., Parazoo, N., Frankenberg, C., and Stutz, J.: Seasonal timing of fluorescence and photosynthetic yields at needle and canopy scales in evergreen needleleaf forests, Ecology, 105, e4402, https://doi.org/https://doi.org/10.1002/ecy.4402, 2024.

Plascyk, J. A. and Gabriel, F. C.: The Fraunhofer Line Discriminator MKII-An Airborne Instrument for Precise and Standardized Ecological Luminescence Measurement, IEEE Transactions on Instrumentation and Measurement, 24, 306–313, https://doi.org/10.1109/TIM.1975.4314448, 1975.

Porcar-Castell, A.: A high-resolution portrait of the annual dynamics of photochemical and non-photochemical quenching in needles of Pinus sylvestris, Physiologia Plantarum, 143, 139–153, https://doi.org/https://doi.org/10.1111/j.1399-3054.2011.01488.x, 2011.

Porcar-Castell, A., Juurola, E., Ensminger, I., Berninger, F., Hari, P., and Nikinmaa, E.: Seasonal acclimation of photosystem II in Pinus sylvestris. II. Using the rate constants of sustained thermal energy dissipation and photochemistry to study the effect of the light environment, Tree Physiology, 28, 1483–1491, https://doi.org/10.1093/treephys/28.10.1483, 2008.

Porcar-Castell, A., Malenovský, Z., Magney, T., Van Wittenberghe, S., Fernández-Marín, B., Maignan, F., Zhang, Y., Maseyk, K., Atherton, J., Albert, L. P., Robson, T. M., Zhao, F., Garcia-Plazaola, J.-I., Ensminger, I., Rajewicz, P. A., Grebe, S., Tikkanen, M., Kellner, J. R., Ihalainen, J. A., Rascher, U., and Logan, B.: Chlorophyll a fluorescence illuminates a path connecting plant molecular biology to Earth-system science, Nature Plants, 7, 998–1009, https://doi.org/10.1038/s41477-021-00980-4, 2021.

Qiu, B., Chen, J. M., Ju, W., Zhang, Q., and Zhang, Y.: Simulating emission and scattering of solar-induced chlorophyll fluorescence at far-red band in global vegetation with different canopy structures, Remote Sensing of Environment, 233, 111 373, https://doi.org/https://doi.org/10.1016/j.rse.2019.111373, 2019.

Quaife, T.: A two stream radiative transfer model for vertically inhomogeneous vegetation canopies including internal emission, Journal of Advances in Modeling Earth Systems, p. to appear, under submission, 2025.

Raczka, B., Porcar-Castell, A., Magney, T., Lee, J. E., Köhler, P., Frankenberg, C., Grossmann, K., Logan, B. A., Stutz, J., Blanken, P. D., Burns, S. P., Duarte, H., Yang, X., Lin, J. C., and Bowling, D. R.: Sustained Nonphotochemical Quenching Shapes the Seasonal Pattern of Solar-Induced Fluorescence at a High-Elevation Evergreen Forest, Journal of Geophysical Research: Biogeosciences, 124, 2005–2020, https://doi.org/https://doi.org/10.1029/2018JG004883, 2019.

Rantanen, M., Karpechko, A. Y., Lipponen, A., Nordling, K., Hyvärinen, O., Ruosteenoja, K., Vihma, T., and Laaksonen, A.: The Arctic has warmed nearly four times faster than the globe since 1979, Communications Earth & Environment, 3, 168, https://doi.org/10.1038/s43247-022-00498-3, 2022.

Reichstein, M., Falge, E., Baldocchi, D., Papale, D., Aubinet, M., Berbigier, P., Bernhofer, C., Buchmann, N., Gilmanov, T., Granier, A., Grünwald, T., Havránková, K., Ilvesniemi, H., Janous, D., Knohl, A., Laurila, T., Lohila, A., Loustau, D., Matteucci, G., Meyers, T., Miglietta, F., Ourcival, J.-M., Pumpanen, J., Rambal, S., Rotenberg, E., Sanz, M., Tenhunen, J., Seufert, G., Vaccari, F., Vesala, T., Yakir, D., and Valentini, R.: On the separation of net ecosystem exchange into assimilation and ecosystem respiration: review and improved algorithm, Global Change Biology, 11, 1424–1439, https://doi.org/https://doi.org/10.1111/j.1365-2486.2005.001002.x, 2005.

Richardson, A. D., Hollinger, D. Y., Burba, G. G., Davis, K. J., Flanagan, L. B., Katul, G. G., William Munger, J., Ricciuto, D. M., Stoy, P. C., Suyker, A. E., Verma, S. B., and Wofsy, S. C.: A multi-site analysis of random error in tower-based measurements of carbon and energy fluxes, Agricultural and Forest Meteorology, 136, 1–18, https://doi.org/https://doi.org/10.1016/j.agrformet.2006.01.007, 2006.

Sabater, N., Vicent, J., Alonso, L., Verrelst, J., Middleton, E. M., Porcar-Castell, A., and Moreno, J.: Compensation of Oxygen Transmittance Effects for Proximal Sensing Retrieval of Canopy–Leaving Sun–Induced Chlorophyll Fluorescence, Remote Sensing, 10, https://doi.org/10.3390/rs10101551, 2018.

Schimel, D., Schneider, F. D., and JPL Carbon and Ecosystem Participants : Flux towers in the sky: global ecology from space, New Phytologist, 224, 570–584, https://doi.org/https://doi.org/10.1111/nph.15934, 2019.

Spitters, C. J. T.: Separating the Diffuse and Direct Component of Global Radiation and Its Implications for Modeling Canopy Photosynthesis .2. Calculation of Canopy Photosynthesis, Agricultural and Forest Meteorology, 38, 231–242, 1986.

Stretton, M. A., Quaife, T., Wilkes, P., and Disney, M.: The influence of 3D canopy structure on modelled photosynthesis, Agricultural and Forest Meteorology, 366, 110 437, 2025.

Sun, Y., Frankenberg, C., Wood, J. D., Schimel, D. S., Jung, M., Guanter, L., Drewry, D. T., Verma, M., Porcar-Castell, A., Griffis, T. J., Gu, L., Magney, T. S., Köhler, P., Evans, B., and Yuen, K.: OCO-2 advances photosynthesis observation from space via solar-induced chlorophyll fluorescence, Science, 358, eaam5747, https://doi.org/10.1126/science.aam5747, 2017.

Sun, Y., Gu, L., Wen, J., Van Der Tol, C., Porcar-Castell, A., Joiner, J., Chang, C. Y., Magney, T., Wang, L., Hu, L., Rascher, U., Zarco-Tejada, P., Barrett, C. B., Lai, J., Han, J., and Luo, Z.: From remotely sensed solar-induced chlorophyll fluorescence to ecosystem structure, function, and service: Part I—Harnessing theory, Global Change Biology, 29, 2926–2952, https://doi.org/10.1111/gcb.16634, 2023a.

Sun, Y., Wen, J., Gu, L., Joiner, J., Chang, C. Y., Van Der Tol, C., Porcar-Castell, A., Magney, T., Wang, L., Hu, L., Rascher, U., Zarco-Tejada, P., Barrett, C. B., Lai, J., Han, J., and Luo, Z.: From remotely-sensed solar-induced chlorophyll fluorescence to ecosystem structure, function, and service: Part II—Harnessing data, Global Change Biology, 29, 2893–2925, https://doi.org/10.1111/gcb.16646, 2023b.

Tanja, S., Berninger, F., Vesala, T., Markkanen, T., Hari, P., Mäkelä, A., Ilvesniemi, H., Hänninen, H., Nikinmaa, E., Huttula, T., Laurila, T., Aurela, M., Grelle, A., Lindroth, A., Arneth, A., Shibistova, O., and Lloyd, J.: Air temperature triggers the recovery of evergreen boreal forest photosynthesis in spring, Global Change Biology, 9, 1410–1426, https://doi.org/https://doi.org/10.1046/j.1365-2486.2003.00597.x, 2003.

Thum, T., Aaalto, T., Laurila, T., Aurela, M., Kolari, P., and Hari, P.: Parametrization of two photosynthesis models at the canopy scale in a northern boreal Scots pine forest, Tellus B, 59, 874–890, https://doi.org/https://doi.org/10.1111/j.1600-0889.2007.00305.x, 2007.

Thum, T., Aalto, T., Laurila, T., Aurela, M., Lindroth, A., and Vesala, T.: Assessing seasonality of biochemical $CO_2$ exchange model parameters from micrometeorological flux observations at boreal coniferous forest, Biogeosciences, 5, 1625–1639, https://doi.org/10.5194/bg-5-1625-2008, 2008.

Thum, T., Aalto, T., Laurila, T., Aurela, M., Hatakka, J., Lindroth, A., and Vesala, T.: Spring initiation and autumn cessation of boreal coniferous forest $CO_2$ exchange assessed by meteorological and biological variables, Tellus B: Chemical and Physical Meteorology, 61, 701, https://doi.org/10.1111/j.1600-0889.2009.00441.x, 2009.

Thum, T., Zaehle, S., Köhler, P., Aalto, T., Aurela, M., Guanter, L., Kolari, P., Laurila, T., Lohila, A., Magnani, F., Van Der Tol, C., and Markkanen, T.: Modelling sun-induced fluorescence and photosynthesis with a land surface model at local and regional scales in northern Europe, Biogeosciences, 14, 1969–1987, https://doi.org/10.5194/bg-14-1969-2017, 2017.

Thum, T., Caldararu, S., Engel, J., Kern, M., Pallandt, M., Schnur, R., Yu, L., and Zaehle, S.: A new model of the coupled carbon, nitrogen, and phosphorus cycles in the terrestrial biosphere (QUINCY v1.0; revision 1996), Geoscientific Model Development, 12, 4781–4802, https://doi.org/10.5194/gmd-12-4781-2019, 2019.

Thum, T., Miinalainen, T., Seppälä, O., Croft, H., Rogers, C., Staebler, R., Caldararu, S., and Zaehle, S.: Modelling decadal trends and the impact of extreme events on carbon fluxes in a temperate deciduous forest using a terrestrial biosphere model, Biogeosciences, 22, 1781–1807, https://doi.org/10.5194/bg-22-1781-2025, 2025.

van der Tol, C., Verhoef, W., Timmermans, J., Verhoef, A., and Su, Z.: An integrated model of soil-canopy spectral radiances, photosynthesis, fluorescence, temperature and energy balance, Biogeosciences, 6, 3109–3129, https://doi.org/10.5194/bg-6-3109-2009, 2009.

van der Tol, C., Berry, J. A., Campbell, P. K. E., and Rascher, U.: Models of fluorescence and photosynthesis for interpreting measurements of solar-induced chlorophyll fluorescence, Journal of Geophysical Research: Biogeosciences, 119, 2312–2327, https://doi.org/10.1002/2014JG002713, 2014.

Van Der Tol, C., Vilfan, N., Dauwe, D., Cendrero-Mateo, M. P., and Yang, P.: The scattering and re-absorption of red and near-infrared chlorophyll fluorescence in the models Fluspect and SCOPE, Remote Sensing of Environment, 232, 111 292, https://doi.org/10.1016/j.rse.2019.111292, 2019.

van der Tol, C., Julitta, T., Yang, P., Sabater, N., Reiter, I., Tudoroiu, M., Schuettemeyer, D., and Drusch, M.: Retrieval of chlorophyll fluorescence from a large distance using oxygen absorption bands, Remote Sensing of Environment, 284, 113 304, https://doi.org/https://doi.org/10.1016/j.rse.2022.113304, 2023.

Van Wittenberghe, S., Amin, E., Pascual-Venteo, A. B., Pérez-Suay, A., Tenjo, C., Sabater, N., Van Der Tol, C., Drusch, M., and Moreno, J.: Retrieval of leaf-level fluorescence quantum efficiency and NPQ-related xanthophyll absorption through spectral unmixing strategies for future VIS-NIR imaging spectroscopy, Remote Sensing of Environment, 300, 113 879, https://doi.org/10.1016/j.rse.2023.113879, 2024.

Vekuri, H., Tuovinen, J.-P., Kulmala, L., Aurela, M., Thum, T., Liski, J., and Lohila, A.: Improved uncertainty estimates for eddy covariance-based carbon dioxide balances using deep ensembles for gap-filling, Agricultural and Forest Meteorology, 371, 110 558, https://doi.org/https://doi.org/10.1016/j.agrformet.2025.110558, 2025.

Verhoef, W.: Light scattering by leaf layers with application to canopy reflectance modeling: The SAIL model, Remote Sensing of Environment, 16, 125–141, https://doi.org/https://doi.org/10.1016/0034-4257(84)90057-9, 1984.

Vesala, T., Launiainen, S., Kolari, P., Pumpanen, J., Sevanto, S., Hari, P., Nikinmaa, E., Kaski, P., Mannila, H., Ukkonen, E., Piao, S. L., and Ciais, P.: Autumn temperature and carbon balance of a boreal Scots pine forest in Southern Finland, Biogeosciences, 7, 163–176, https://doi.org/10.5194/bg-7-163-2010, 2010.

Vilfan, N., van der Tol, C., Muller, O., Rascher, U., and Verhoef, W.: Fluspect-B: A model for leaf fluorescence, reflectance and transmittance spectra, Remote Sensing of Environment, 186, 596–615, https://doi.org/https://doi.org/10.1016/j.rse.2016.09.017, 2016.

Vilfan, N., Van der Tol, C., Yang, P., Wyber, R., Malenovský, Z., Robinson, S. A., and Verhoef, W.: Extending Fluspect to simulate xanthophyll driven leaf reflectance dynamics, Remote Sensing of Environment, 211, 345–356, https://doi.org/https://doi.org/10.1016/j.rse.2018.04.012, 2018.

Walther, S., Voigt, M., Thum, T., Gonsamo, A., Zhang, Y., Köhler, P., Jung, M., Varlagin, A., and Guanter, L.: Satellite chlorophyll fluorescence measurements reveal large-scale decoupling of photosynthesis and greenness dynamics in boreal evergreen forests, Global Change Biology, 22, 2979–2996, https://doi.org/10.1111/gcb.13200, 2016.

Wang, J., Jiang, F., Wang, H., Qiu, B., Wu, M., He, W., Ju, W., Zhang, Y., Chen, J. M., and Zhou, Y.: Constraining global terrestrial gross primary productivity in a global carbon assimilation system with OCO-2 chlorophyll fluorescence data, Agricultural and Forest Meteorology, 304-305, 108 424, https://doi.org/https://doi.org/10.1016/j.agrformet.2021.108424, 2021.

Wang, N., Yang, P., Clevers, J. G., Wieneke, S., and Kooistra, L.: Decoupling physiological and non-physiological responses of sugar beet to water stress from sun-induced chlorophyll fluorescence, Remote Sensing of Environment, 286, 113 445, https://doi.org/https://doi.org/10.1016/j.rse.2022.113445, 2023.

Willmott, C. J.: On the validation of models, Physical Geography, 2, 184–194, https://doi.org/10.1080/02723646.1981.10642213, 1981.

Wright, S.: Correlation and Causation, Journal of Agricultural Research, 20, 557–585, 1921.

Wutzler, T., Lucas-Moffat, A., Migliavacca, M., Knauer, J., Sickel, K., Šigut, L., Menzer, O., and Reichstein, M.: Basic and extensible post-processing of eddy covariance flux data with REddyProc, Biogeosciences, 15, 5015–5030, https://doi.org/10.5194/bg-15-5015-2018, 2018.

Yang, P., Verhoef, W., and van der Tol, C.: The mSCOPE model: A simple adaptation to the SCOPE model to describe reflectance, fluorescence and photosynthesis of vertically heterogeneous canopies, Remote Sensing of Environment, 201, 1–11, https://doi.org/https://doi.org/10.1016/j.rse.2017.08.029, 2017.

Yang, P., Prikaziuk, E., Verhoef, W., and van der Tol, C.: SCOPE 2.0: a model to simulate vegetated land surface fluxes and satellite signals, Geoscientific Model Development, 14, 4697–4712, https://doi.org/10.5194/gmd-14-4697-2021, 2021.

Yang, P., Liu, Z., Han, D., Zhang, R., Siegmann, B., Liu, J., Zhao, H., Rascher, U., Chen, J. M., and van der Tol, C.: Mitigating the black-soil problem in the reflectance-to-fluorescence (R2F) relationship: A soil-adjusted reflectance-based approach for downscaling SIF, Remote Sensing of Environment, 330, 114 998, https://doi.org/https://doi.org/10.1016/j.rse.2025.114998, 2025a.

Yang, P., van der Tol, C., Liu, J., and Liu, Z.: Separation of the direct reflection of soil from canopy spectral reflectance, Remote Sensing of Environment, 316, 114 500, https://doi.org/https://doi.org/10.1016/j.rse.2024.114500, 2025b.

Zaks, J., Amarnath, K., Sylak-Glassman, E. J., and Fleming, G. R.: Models and measurements of energy-dependent quenching, Photosynthesis Research, 116, 389–409, https://doi.org/10.1007/s11120-013-9857-7, 2013.

Zeng, Q., Wu, X., Tang, R., Wang, J., Lin, X., Wen, J., and Xiao, Q.: Quantification of uncertainty caused by geometric location mismatch in the validation of TROPOMI solar-induced chlorophyll fluorescence product, International Journal of Digital Earth, 17, 2330 688, https://doi.org/10.1080/17538947.2024.2330688, 2024.

Zeng, Y., Badgley, G., Dechant, B., Ryu, Y., Chen, M., and Berry, J.: A practical approach for estimating the escape ratio of near-infrared solar-induced chlorophyll fluorescence, Remote Sensing of Environment, 232, 111 209, https://doi.org/10.1016/j.rse.2019.05.028, 2019.

Zeng, Y., Badgley, G., Chen, M., Li, J., Anderegg, L. D., Kornfeld, A., Liu, Q., Xu, B., Yang, B., Yan, K., and Berry, J. A.: A radiative transfer model for solar induced fluorescence using spectral invariants theory, Remote Sensing of Environment, 240, 111 678, https://doi.org/https://doi.org/10.1016/j.rse.2020.111678, 2020.

Zhang, Y., Xiao, X., Zhang, Y., Wolf, S., Zhou, S., Joiner, J., Guanter, L., Verma, M., Sun, Y., Yang, X., Paul-Limoges, E., Gough, C. M., Wohlfahrt, G., Gioli, B., van der Tol, C., Yann, N., Lund, M., and de Grandcourt, A.: On the relationship between sub-daily instantaneous and daily total gross primary production: Implications for interpreting satellite-based SIF retrievals, Remote Sensing of Environment, 205, 276–289, https://doi.org/https://doi.org/10.1016/j.rse.2017.12.009, 2018.

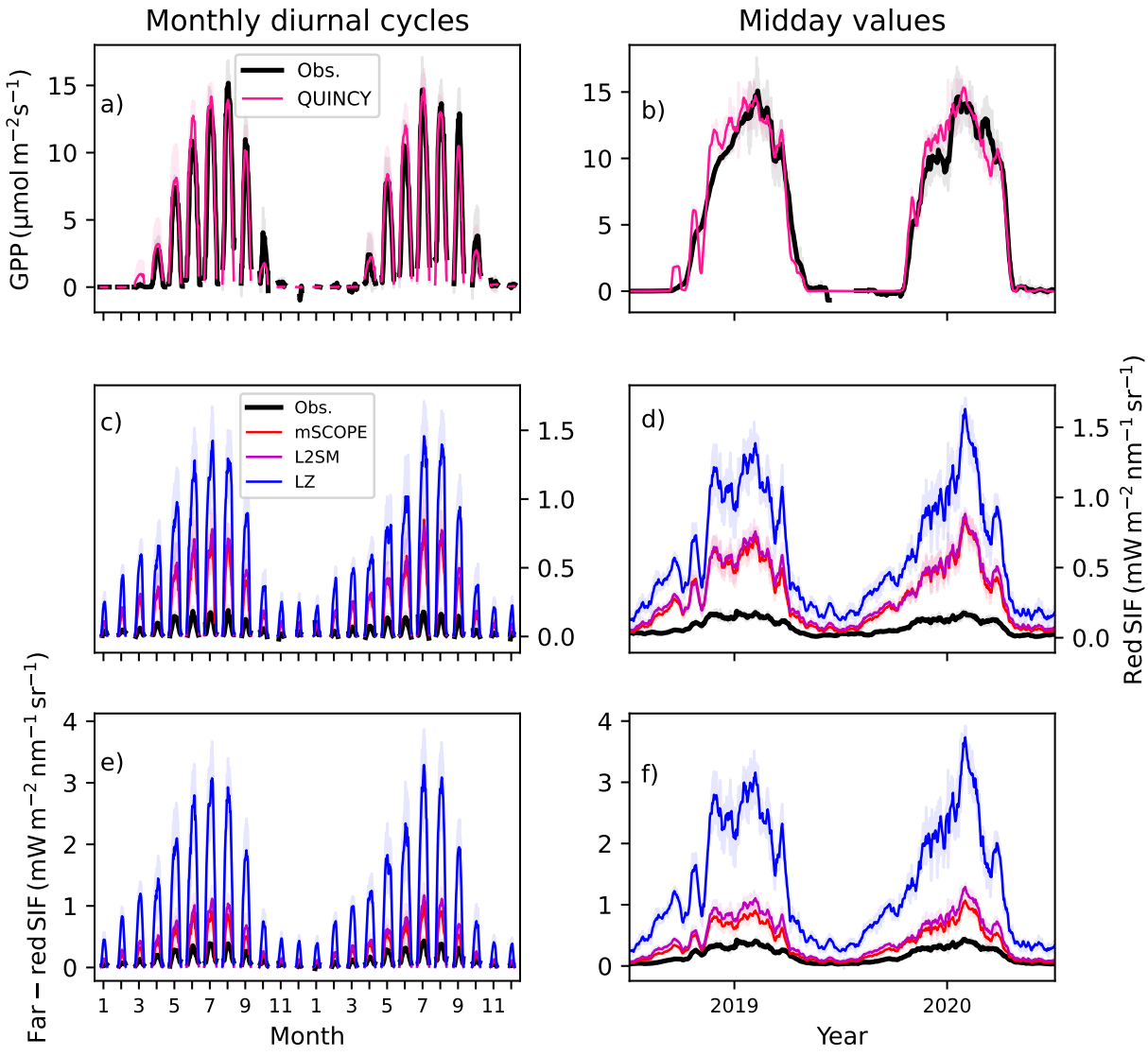


**Figure 3.** Monthly diurnal cycles for ~~GPP~~ (a) GPP, ~~red region SIF~~ (c) ~~and far-red~~ red region SIF and (e) far-red SIF and midday values, calculated from winter time between 10 a.m. and 1:30 p.m., for ~~GPP~~ (b) GPP, ~~red region SIF~~ (d) ~~and far-red~~ red region SIF and (f) far-red SIF in CA-Obs. The black line is the observation in all plots, the pink line in the GPP plots is the QUINCY simulation. For the SIF plots the red line is the mSCOPE result, magenta the L2SM and blue the LZ approach. All the lines for midday values have been smoothed with a 15-day long window.

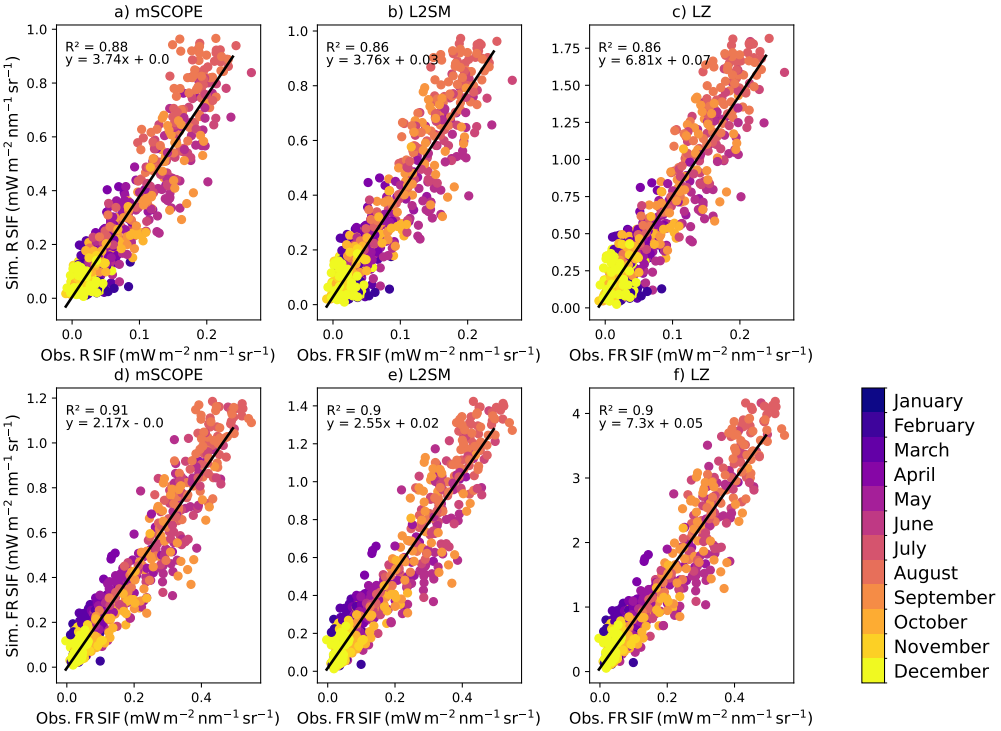


**Figure 4.** Observed vs. modelled SIF midday values in the red (denoted with R in the figure) region (~~QUINCY-mSCOPE:~~ a~~, Q-L2SM~~: ~~b~~mSCOPE, ~~Q-LZ~~b: ~~e~~L2SM, ~~upscaled~~c: ~~d~~LZ) and far-red (denoted with FR in the figure) region (~~QUINCY-mSCOPE~~d: ~~e~~mSCOPE, ~~Q-L2SM~~e: L2SM: f~~, Q-LZ~~: ~~g~~LZ) at CA-Obs. Values from different months are color-coded. The black line shows a fit with the corresponding parameters shown in each panel.

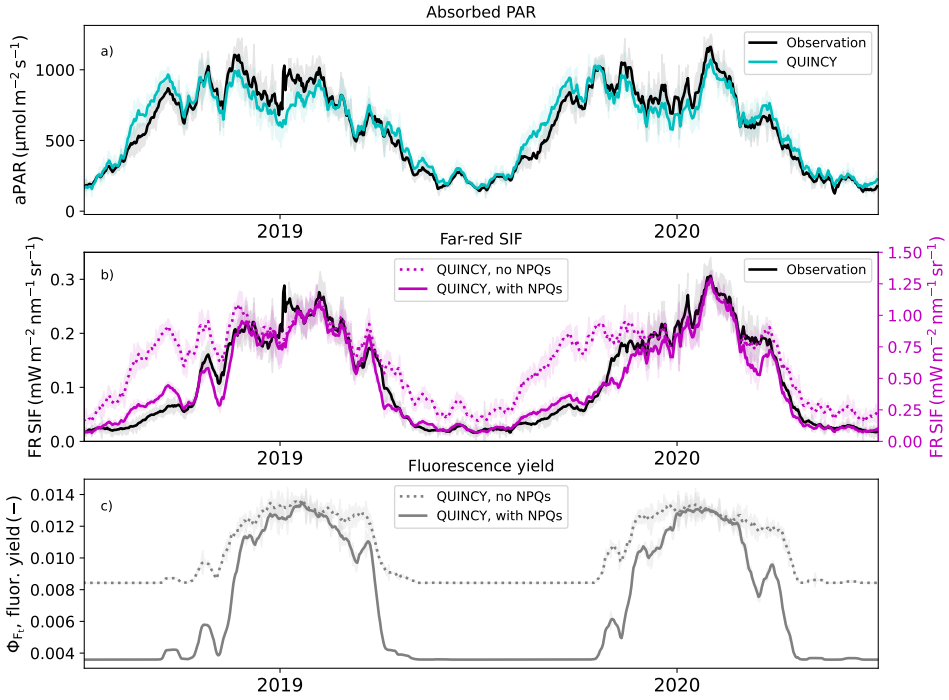


**Figure 5.** (a) The observed and simulated absorbed photosynthetically active radiation at CA-Obs, (~~a~~b) ~~, near-infrared~~ far red (FR) region SIF values with and without sustained NPQ simulated with L2SM and (~~b~~c) ~~and~~ simulated chlorophyll fluorescence yields with and without sustained NPQ~~(c)~~. Values are averages of midday values (10 a.m. to 1:30 p.m.), the standard deviation is shown as shaded areas. All the lines for midday values were smoothed with a 15-day long window.

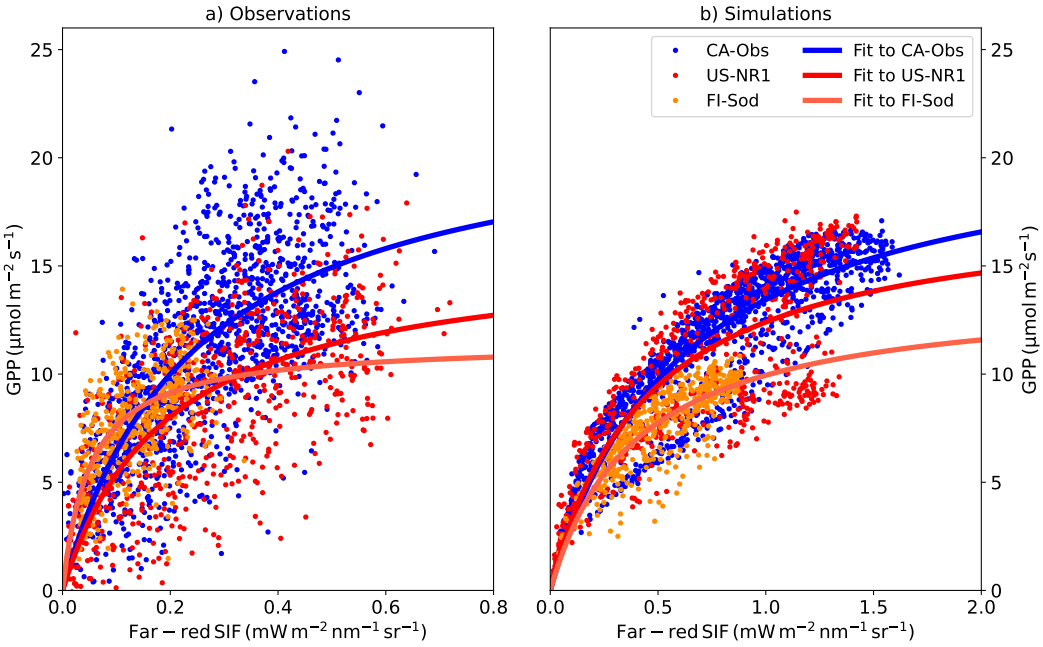


**Figure 6.** ~~The observed~~ (a) The observed and ~~simulated~~ (b) simulated GPP vs. far-red region SIF relationship at three different sites for half-hourly values for all points in June and July using the L2SM approach in the simulations. CA-Obs has half-hourly values and FI-Sod and US-NR1 hourly values. ~~The values before noon are denoted as dots, the values after noon are denoted as crosses.~~ Hyperbolic fits are shown as solid lines in the figure.

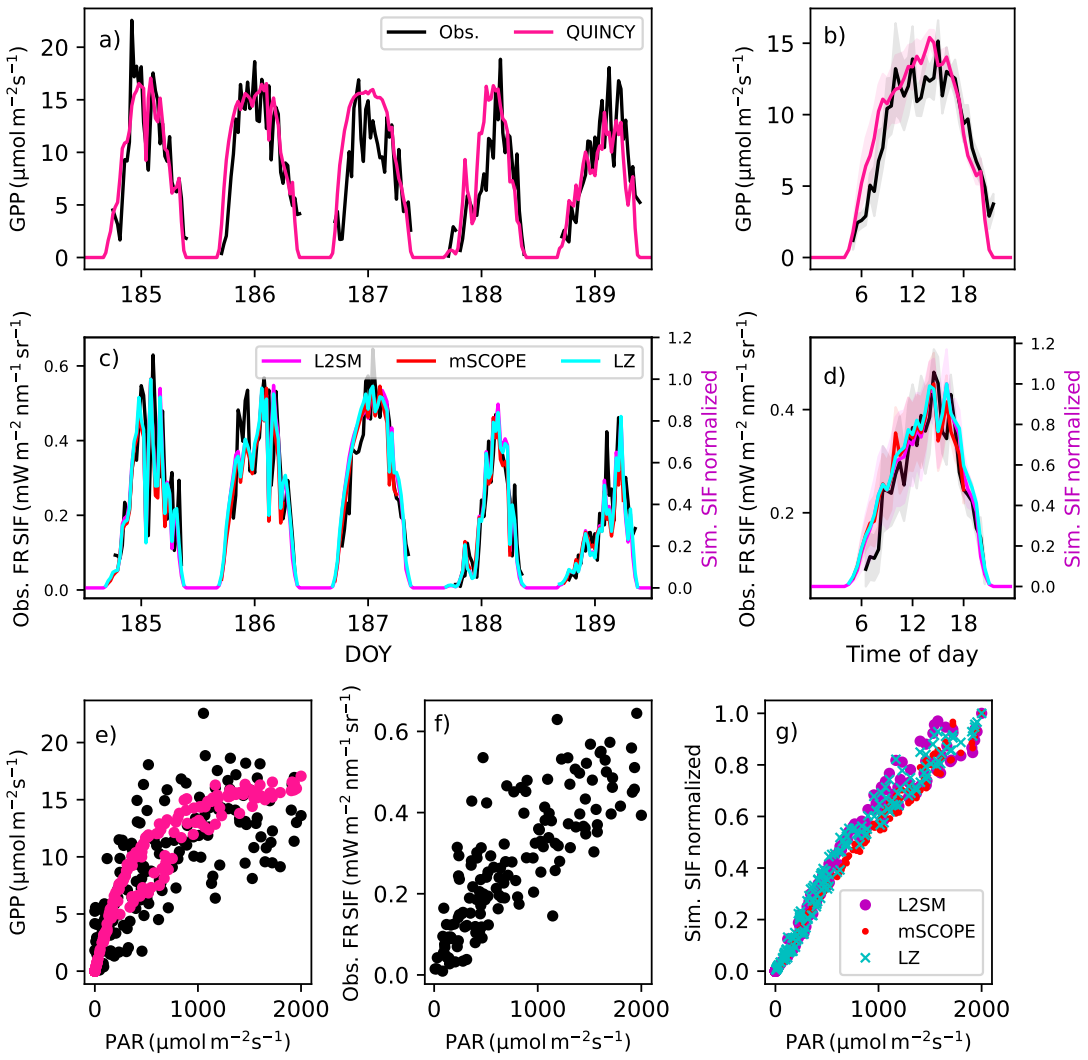


**Figure 7.** (a) The observed and simulated GPP and (~~a~~c) ~~and~~ far-red ~~region SIF~~ (~~e~~denoted as FR in the figure) region SIF for days 185-189 (5 July-8 July 2020) and averaged over these five days (b for GPP and d for far-red region SIF) at CA-Obs. The shaded regions in b and d show the standard deviations of the averaged values. (e) The light response of the observed and simulated GPP for these five days, (e~~f~~) ~~,~~the observed far-red region SIF ~~(f)~~ and the (g) simulated far-red region SIF~~(g)~~. The observations are in black, the simulated GPP is in pink and the simulated far-red SIF from L2SM is in magenta, from mSCOPE in red and from ~~Zeng~~ LZ approach in cyan. The simulated SIF values have been normalized to one.

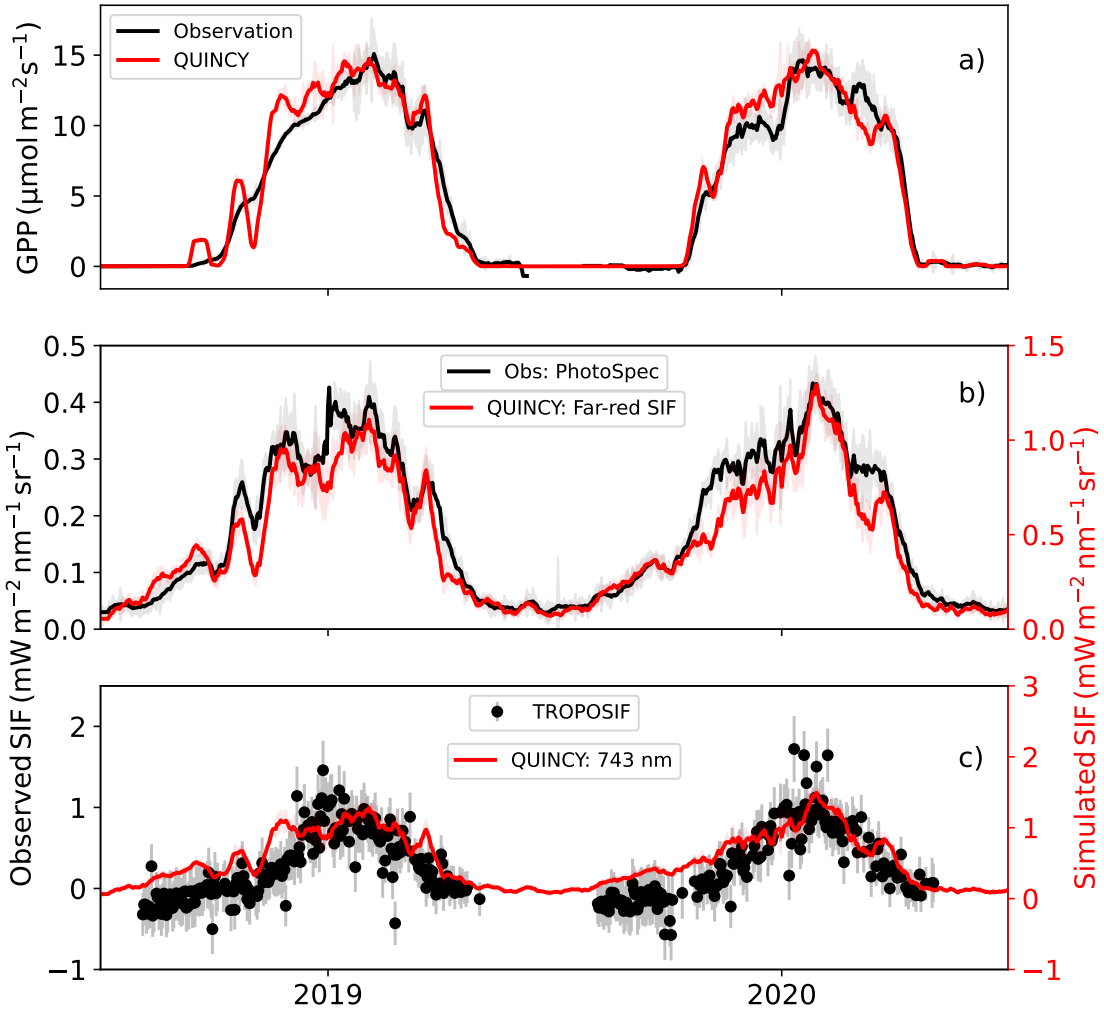


**Figure 8.** ~~The~~ In (a) the observed and simulated GPP at CA-Obs, (~~a~~b) ~~,~~ near-infrared SIF from PhotoSpec observations and simulations with L2SM and (~~b~~c) and TROPOSIF observations and simulations with L2SM at 743 nm~~(c)~~. The other values than TROPOSIF are averages of midday (10 a.m. to 1:30 p.m.) values, with standard deviation is shown as shaded areas and TROPOSIF uncertainty from the retrievals shown in error bars (c). TROPOSIF values are daily. All the lines for midday values have been smoothed with a 15-day long window.